THE MONTE CARLO TECHNIQUES WITH PULSE COMPRESSION
FOR ROUGH SURFACE SCATTERING

by

Jun Yan

B.S., Electronic Engineering
Zhejiang University, 1990

M.S., Electrical Engineering
University of Mississippi, 1992

Submitted to the Department of Electrical Engineering and Computer
Science and the Department of Ocean Engineering in Partial
Fulfillment of the Requirements for the Degrees of

Master of Science in Electrical Engineering and Computer Science
and
Master of Science in Ocean Engineering

at the

MASSACHUSETTS INSTITUTE OF TECHNOLOGY
June 1996

© Massachusetts Institute of Technology 1996

Signature of Author _____
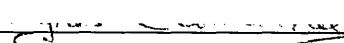Department of Ocean Engineering   May 1996

Certified by _____
Y. Eric Yang, Research Scientist, Research Laboratory of Electronics
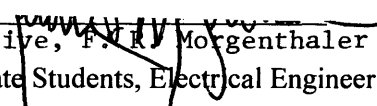Thesis Supervisor

Certified by _____
Henrik Schmidt, Professor of Ocean Engineering
Thesis Supervisor

Accepted by _____
A.D. Carmichael
Chairman, Department Committee on Graduate Students, Ocean Engineering

Accepted by _____
Alvin W. Drake, C.G.S.P. Representative, F.R. Morgenthaler
Chairman, Department Committee on Graduate Students, Electrical Engineering
and Computer Science

THE MONTE CARLO TECHNIQUES WITH PULSE COMPRESSION FOR ROUGH SURFACE SCATTERING

by

Jun Yan

Submitted to the Department of Electrical Engineering and Computer Science and the Department of Ocean Engineering in Partial Fulfillment of the Requirements for the Degrees of

Master of Science in Electrical Engineering and Computer Science
and
Master of Science in Ocean Engineering

ABSTRACT

Radar scattering from random rough surface can be calculated using method of moment in combination with the Monte Carlo simulation technique. One of the practical limitation to this approach is that a tapered plane wave must be synthesized in order to limit the illuminated surface area so that computational domain would be confined. However, at grazing angle incidence, the tapered plane wave alone will not do enough to limit the illuminated area. In this thesis, we propose to use a pulse compression technique in the longitudinal direction. This approach will be more effective in limiting the illuminated area at low grazing incidence angles. Numerical simulation results will be obtained and compared with those from the analytical expression at small perturbation condition.

Thesis Supervisor: Y. Eric Yang

Title: Research Scientist, Research Laboratory of Electronics

Thesis Supervisor: Henrik Schmidt

Title: Professor of Ocean Engineering

Acknowledgment

To Professor Jin Au Kong for his very impressive teaching, excellent research leadership and letting me join the group in the beginning.

To Dr. Y. Eric Yang for his patience and enthusiasm to put ideas to work as well as helping me through all the research work which leads to the final form of this thesis.

To Professor Henrik Schmidt for his great help as my academic advisor.

To Dr. Robert T. Shin for his helpful and illuminating discussion.

To Chih-Chien Hsu, for his constructive suggestion, discussion and sincere help.

To J. T. Johnson for his great support and help on using his program.

To all the friends in my group.

To all those people, who have helped me along the trace of my life, who have passed away and who are still with me, in this world.

To all my friends.
And
to my family.

Table of Contents

List of Figures

List of Tables

Chapter 1 Introduction

Numerical analysis of electromagnetic wave scattering by random rough surfaces has been investigated using integral equations such as Kirchhoff Approximation, Small Perturbation Method [1], Padé Approximants [2], and partial differential equations [3]. Among the integral equation simulations, Method of Moments (MOM) [4] is a popular tool due to its inclusion of multiple scattering. It is noted, however, that the simulation technique becomes very time consuming at low grazing angle incidence. This is because computational domain expands significantly compared to near-normal incidence. In practice, it is also difficult to obtain controlled measurement results to validate theoretical predictions, which requires the radar beam to illuminate only one type of surface over a long range.

Several algorithms have been proposed to counter this grazing angle incidence problem in numerical simulation as well as in experimental measurement. In Beam Simulation Method (BSM) [5] and [6], the incident beam is first decomposed into subbeams and the scattered field due to the large beam illumination is synthesized by coherent superposition of the subbeam results. This algorithm makes it easier to decompose the computing job for parallel or distributed systems, thus to increase the processing speed. However, the grazing incidence angle can only go as far as 80 degrees and the multiple scattering between individual beams is not in the consideration. Another area limiting technique, 2D wave tapering is used to limit the illumination area. At small angle of incidence, this technique works well. Unfortunately, at grazing angle, the tapered area will increase along the direction of incidence and give rise to the same difficulty mentioned above.

Recent advances in signal processing hardware have made high-resolution imaging radar a reality. An important feature of these imaging radar systems is that since range resolution is determined by the signal processing algorithm such as the pulse compression technique [7] - [8] and range gating, the effective illuminated area corresponding to an image pixel can be limited even at very low grazing angle incidence. Our work is motivated by this type of radar applications. The rough surface is assumed to have fixed size, as determined by the limitation of the computational technique. For each randomly generated surface, we obtain the range-gated scattering return using plane wave pulse illumination. The effective pulse width is chosen to fit within the range direction of the surface so that the edge effect can be minimized. In order to do so, backscattering cross sections at multiple frequency steps from different surfaces are averaged to obtain the mean normalized radar cross section, using MOM. The computed results in frequency domain is then resynthesized into time domain and time gating (or the range gating) is finally performed to discriminate the scattering surface segment of interest. To verify the correctness of the scheme, the RCS of the scattering plate is obtained at small perturbation condition and is compared to the analytical results.

The problem of plane wave pulse scattering from rough surface is outlined in Chapter 2, together with the introduction to related methodologies such as MOM, the Monte Carlo simulation, the pulse compression technique, range gating and RCS calculation. In Chapter 3, we investigate and propose our scheme to deal with the special case of 1D surface. Here, the tapering is no longer necessary due to the pulse area limiting effect itself. The pulse scattering return in time is obtained by running the simulation model at multiple frequencies and then performing the Fourier synthesis. The simulation steps and results are presented in Chapter 4, where we carefully set up testing cases, verify the range gating idea. Finally, we discuss the Monte Carlo simulation procedures

and compare the RCS with that obtained from SPM. In Chapter 5, we summarize the research work and propose 2D area limitation scheme as our future work.

Chapter 2 Problem Definition and Related Methodologies

In this chapter, we will define the grazing angle scattering problem to be solved, briefly propose a solution scheme and discuss the related methodologies such as the MOM, Monte Carlo simulations, pulse compression techniques, range gating and RCS calculation.

2.1 Problem Definition and Solution Technique

Fig. 1 shows a plane wave pulse incident on a 1D rough surface plate at grazing incident angle θ. The profile of the rough surface and the pulse duration are known. The problem is to find the scattering return from segment x_1-x_2 due to this pulse incidence.

We will solve this problem using the MOM technique over the pulse bandwidth. The first step is to decompose the incident pulse into individual frequency components. Then the scattering at these individual components are calculated using MOM. The correspondent time signal can be resythesized using the inverse Fourier transform. Finally, the scattering due to segment x_1-x_2 can be obtained by gating the time return. The detail is presented in later sections.
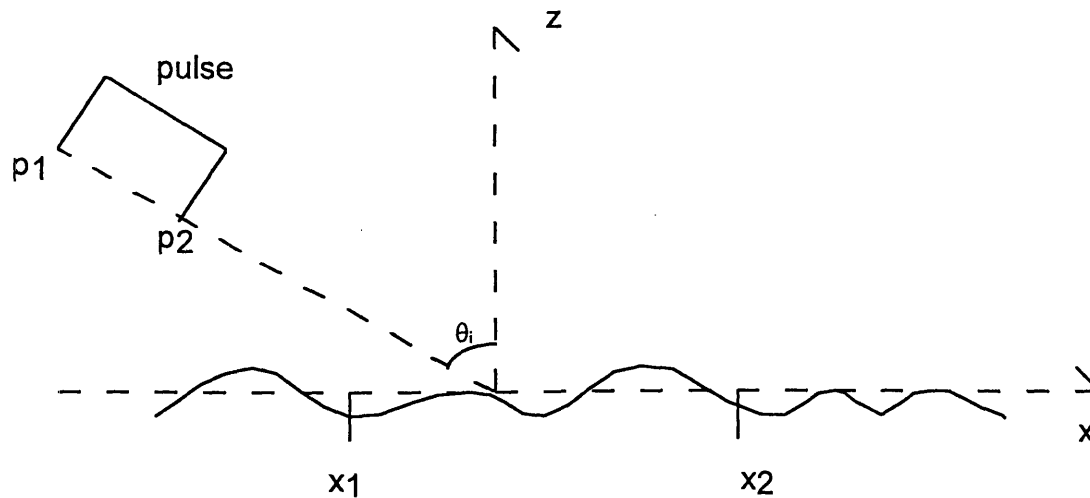
Fig.1 Plane wave pulse rough surface scattering using range gating.

2.2 The Method of Moment

The numerical simulation of the electromagnetic scattering usually falls into one of the two categories, the integral equation method and the differential equation method. The differential equation method include Finite Difference (FD) method in either time or frequency domain which has been used in many applications such as rough surface scattering [3]. The FD method in time or frequency domain [9-10] has been widely used to solve open region scattering problem. This method together with the Finite Element Method (FEM) [11-13] is called the finite method due to their application in the finite region. The advantage of the so called finite method is the handling of Inhomogeneous medium. On the boundary, the MOM in integral equation modeling can be used. From simulation experience, the MOM needs only about 7 points per wavelength in order to perform a sound simulation while the FD method requires around 20 points per wavelength. Also, MOM algorithm automatically includes multiple scattering among the surface segments.

There are three major steps in the MOM simulation. The first step is to establish the integral equations on the surface boundary. Two kinds of integral equations can be formulated, i.e., the Electric Field Integral Equation (EFIE) and the Magnetic Field Integral Equation (MFIE). As an example, we present the EFIE simulation for a perfectly conducting surface to illustrate the simulation process.

Suppose we have a perfectly conducting surface illuminated by the incident field $\overline{E}^i$. Let the scattered field be denoted by $\overline{E}^s$. Since for the perfect conductor, the electric field on the surface is zero, we have

$$\overline{E}^s + \overline{E}^i = 0 \tag{1}$$

Let us rewrite (1) as

$$\overline{E}^s = -\,\overline{E}^i \tag{2}$$

The scattered field can be expressed in terms of the dyadic Green's function $\overline{\overline{g}}(\overline{r},\overline{r}')$ and the surface current $\overline{J}(\overline{r}')$.

$$\overline{E}^s = i\,\omega\,\mu \int \int ds'\; \overline{\overline{g}}(\overline{r},\overline{r}') \cdot \overline{J}(\overline{r}') \tag{3}$$

The surface current can be expanded in terms of base functions as

$$\overline{J}(\overline{r}') = \sum_{n} x_n \overline{B}_n(\overline{r}') \tag{4}$$

where x denotes the unknown coefficient to be solved and $\overline{B}$ is the base function. Once the coefficients are determined, the surface current can be obtained and the scattered field will also be known. Substituting (4) into (3), we have

$$\overline{E}^s = \sum_n x_n \, i \, \omega \, \mu \int \int ds'_n \, \vec{g}(\vec{r},\vec{r}') \cdot \overline{B}_n(\vec{r}') \tag{5}$$

We can multiply the two sides of (2) by test functions, take the surface integration and obtain

$$\int \int ds'_m \, \overline{T}_m(\vec{r}') \overline{E}^s = - \int \int ds'_m \, \overline{T}_m(\vec{r}') \overline{E}^i \tag{6}$$

Substitution of (5) into (6) gives

$$\sum_n x_n \, i \, \omega \, \mu \int \int ds'_n \, \vec{g}(\vec{r},\vec{r}') \cdot \overline{B}_n(\vec{r}') \cdot \int \int ds'_m \, \overline{T}_m(\vec{r}') = - \int \int ds'_m \, \overline{T}_m(\vec{r}') \cdot \overline{E}^i \tag{7}$$

Equation (7) can be written in the matrix form as

$$A \, X = B \tag{8}$$

While the element in X is the surface current coefficient we are going to find, the element in A and B can be written as,

$$a_{mn} = i \, \omega \, \mu \int \int ds'_n \, \overline{\overline{g}}(\vec{r},\vec{r}') \cdot \overline{B}_n(\vec{r}') \cdot \int \int ds'_m \, \overline{T}_m(\vec{r}') \tag{9}$$

$$b_m = - \int \int ds'_m \, \overline{T}_m(\vec{r}) \cdot \overline{E}^i \tag{10}$$

One of the major advantage of MOM lies in this process of expansion and testing to set up the matrix equation, since when calculating the surface field on each segment (testing), the scattering effect due to other segments is automatically taken into consideration (expansion). Therefore, the multiple scattering is included in the formulation. The number of unknowns is equal to the number of segments along the surface because on each segment, we have only one coefficient to solve. The formulation above is called the Electric Field Integral Equation (EFIE). Another kind of formulation, Magnetic Field Integral Equation (MFIE) can be found in literature. Once the surface current is determined, the scattered field can be calculated as given in (5). For two dimensional scattering problem, it is usually necessary to have six to seven segments per wavelength.

In our simulation for one dimensional perfect conductor rough surface scattering, we use EFIE as our modeling formulation for the perfect conducting random rough surface scattering.

2.3 Monte Carlo Simulation

Since the rough surface we use to perform the scattering simulation satisfies a certain statistical distribution, the scattered field consists of coherent part and noncoherent part, which can be expressed as

$$E = <E> + e \tag{11}$$

where $<E>$ and e are, respectively, the coherent and noncoherent components. By definition, the noncoherent (or fluctuation) component of the scattered field will have zero mean

$$E= <E> + e \Rightarrow <E>= <E> + <e> \Rightarrow <e> = 0 \qquad (12)$$

What we are really interested in is the second moment of the noncoherent component, $<e^2>$.

For random rough surface with known correlation length and rms height, we can calculate the scattering from different realizations and average the final results to obtain the estimation of the second moment, $<e^2>$. This technique is known as the Monte Carlo method [14-15].

Now, the question is how many surface realizations we should use. To investigate this, we perform some numerical experiments using the simulation scheme that will be discussed in detail in later sections. The projection of the rough surface is 300λ , with λ as the carrier wavelength. Due to the processing capacity of the computer running MOM program, we choose 4 points per wavelength, which is about the marginal number for accurate simulation using MOM. The incident angle is 75 degrees. The rough surface is characterized by 0.04λ rms height and 0.4λ as the correlation length. We plot out, in Fig. 2, the averaged RCS with respect to the number of rough surface realizations. As can be seen, the averaged RCS converges as the number of the surface realizations increases. From this experiment, we can determine the number of realizations for our simulation.
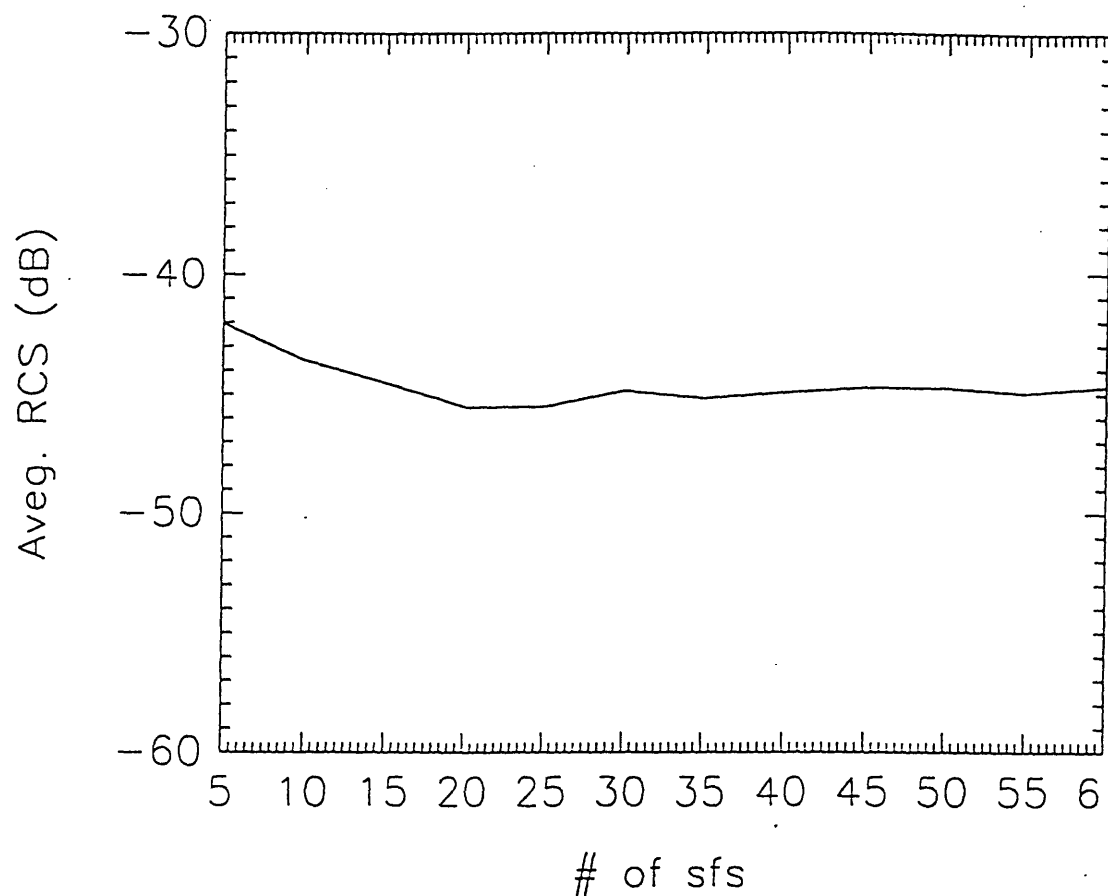
Fig. 2 The Monte Carlo simulation methods of RCS for 60 surface realizations.

2.4   Pulse Compression

The average transmitted power of a given radar may be raised by increasing the pulse length within the given transmitter constraints. However, increasing pulse length has an undesirable effect of decreasing the bandwidth of the received signal, which reduces the range resolution capability of the radar. To achieve this compromise of increasing SNR while keeping bandwidth, a   long pulse containing some sort of phase or frequency

modulation is transmitted. Upon reception, the pulse must be compressed to permit separation of adjacent range resolution cells. The frequency modulation technique is described as follows:

Let transmitted pulse be expressed by

$$P(t) = cos(2 \pi f t) [u(t) - u(t-\tau)] \qquad (13)$$

where

$$f = f_{min} + \frac{(f_{max} - f_{min}) t}{\tau}$$

Here $u(t)$ is the step function and f_{max}, f_{min} are the maximum and minimum modulation frequencies, respectively. Without considering the phase change, the returned pulse from the object at the receiver has similar form

$$P_r (t_r) = A \, cos(2\pi t_r) [u(t_r) - u(t_r - \tau)] \qquad (14)$$

in which P_r denotes the returned pulse, t_r is the time scale for the returned signal and A is the attenuated amplitude, .

At the receiver, the returned signal is further processed so that the delayed time is linear with respect to frequency. The delayed time amount $D(f)$ satisfies the following equation

$$D(f)=T \left(1 - \frac{f-f_{min}}{f_{max} - f_{min}}\right) [u(f-f_{min}) - u(f-f_{max})] \qquad (15)$$

So the pulse at the output of the delayed network is given by

$$P_0 (t') = A \cos(2\pi t')[u(t') - (t'-\tau)], \quad t'=t_r-D(f) \qquad (16)$$

Since the initial returned signal starts with minimum frequency component of maximum delay of T and terminates with maximum frequency component of minimum delay of 0, the effective pulse width is $\tau-T$. Illustrated in Fig. 3 [7] is the transmitted signal using linearly frequency modulation and in Fig. 4 [7] is the received and processed signal.
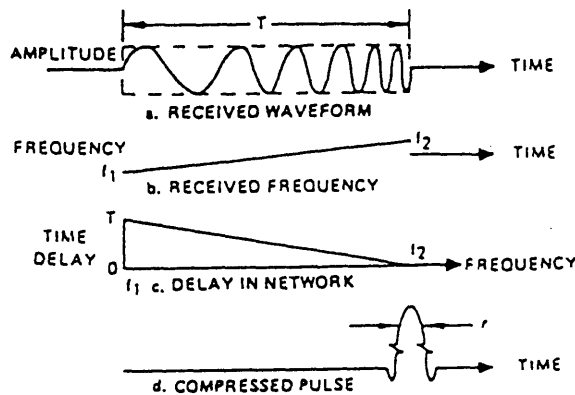
Fig. 3 Transmitted waveform of a linear FM pulse.
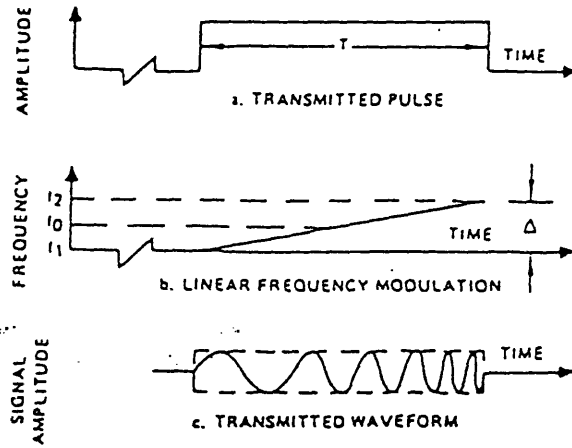
Fig. 4 Received waveform of the FM pulse and subsequent pulse

· compression.

In radar signal processing, the pulse compression technique is often implemented with time gating or range gating to distinguish the scattering segment of interest. In our simulation, however, we will use continuous time plane wave at multiple frequencies to achieve the finite pulse effect.

A typical continuous plane wave can be expressed in time domain as

$$w(t) = A(\omega_n) \ cos \ \omega_n \ (t - \bar{k} \cdot \bar{r} / c) \qquad (17)$$

where ω is the radian frequency, c is the speed of light, t is the time, $\bar{k}$ is the unit vector in the propagation direction and $\bar{r}$ denotes the space location. Our pulse compression scheme is to find, at different frequencies, the continuous time plane waves as shown in

(17) such that their combination is equivalent to a finite-duration plane wave pulse. This process can be achieved through the Fourier analysis and synthesis. Suppose we want to obtain the plane wave pulse of carrier frequency ω given in (18)

$$ps(\bar{r}, t) = \cos \omega_0 (t - \bar{k} \cdot \bar{r} / c) [u(t - \bar{k} \cdot \bar{r} / c + \tau/2) - u(t - \bar{k} \cdot \bar{r} / c - \tau/2)] \qquad (18)$$

The first step is to find its Fourier transform. Noticing that the term $\bar{k} \cdot \bar{r} / c$ in (18) is just the time shift due to different space locations in the direction of incidence, we first find the Fourier transform of the sinusoidal term and the rectangular pulse term.

$$f_1(t) = \cos \omega_0 t \quad \Leftrightarrow \quad F_1(\omega) = \pi [\delta(\omega + \omega_0) + \delta(\omega - \omega_0)] \qquad (19)$$

and

$$f_2(t) = [u(t + \tau/2) - u(t - \tau/2)] \quad \Leftrightarrow \quad F_2(\omega) = \frac{2 \sin \omega \frac{\tau}{2}}{\omega} \qquad (20)$$

Let

$$ps_o(t) = \cos(\omega_o t) [u(t + \tau/2) - u(t - \tau/2)] \qquad (21)$$

Its Fourier transform can be obtained by convoluting (19) and (20) as

$$PS_o(\omega) = \frac{1}{2\pi} F_1(\omega) \otimes F_2(\omega) = \frac{\sin (\omega + \omega_o) \frac{\tau}{2}}{(\omega + \omega_o)} + \frac{\sin (\omega - \omega_o) \frac{\tau}{2}}{(\omega - \omega_o)} \qquad (22)$$

Since $ps(\overline{r}, t)$ is just the time shifted signal of $ps_o(t)$, we can write the Fourier transform of $ps(\overline{r}, t)$ as

$$PS\,(\overline{r},\omega) = e^{i\omega \overline{k}\cdot\overline{r}/c}\,[\,\frac{\sin\,(\omega+\omega_0)\frac{\tau}{2}}{(\omega+\omega_0)} \,+\, \frac{\sin\,(\omega-\omega_0)\frac{\tau}{2}}{(\omega-\omega_0)}\,] \qquad (23)$$

With the knowledge of the frequency spectrum of the desired pulse signal, we can simulate the pulse by using continuous wave at different frequencies and construct the scattered time signal by performing the Fourier synthesis. That is, for an incident wave $PS\,(\overline{r},\omega)$, we calculate the correspondent scattered wave $SC\,(\overline{r},\omega)$ at that particular frequency and obtain the scattered pulse signal in time. This process is shown as following,

since

$$ps(\overline{r},t) = \frac{1}{2\pi}\int d\omega\, PS\,(\overline{r},\omega)\,e^{-i\omega t} \qquad (24)$$

and since

$$PS\,(\overline{r},\omega)\,\Rightarrow\,SC\,(\overline{r},\omega)$$

we can obtain the scattered pulse signal as

$$sc(\overline{r},t) = \frac{1}{2\pi}\int d\omega\, SC\,(\overline{r},\omega)\,e^{-i\omega t} \qquad (25)$$

In summary, the scattered pulse signal is obtained through the use of continuous waves at different frequencies and performing time synthesis. This process is similar to the signal processing scheme discussed at the beginning of the section in that we operate in the frequency domain in order to achieve the desired effect in time.

2.5   Plane Wave Pulse

The understanding of the plane wave pulse is important in our application since we depend on its area limiting effect to truncate the large rough surface.

Here, we want to establish the relation between pulse width and illuminated area. Let's rewrite (18) as

$$ps(\bar{r}, t) = \cos \omega_o (t - \bar{k} \cdot \bar{r} / c) \, [u(t - \bar{k} \cdot \bar{r} / c + \tau/2) - u(t - \bar{k} \cdot \bar{r} / c - \tau/2)]$$

This is in fact the expression for the rectangular plane wave pulse, with carrier frequency. Fig. 5 gives the indication for this plane wave pulse.
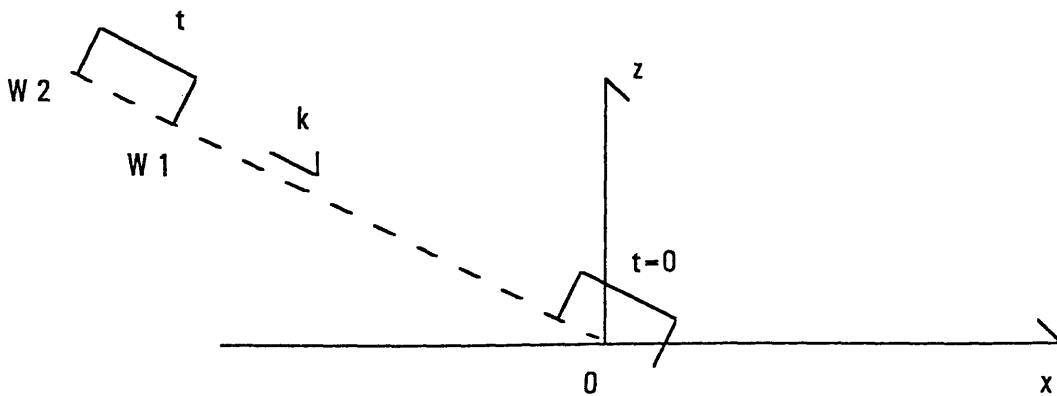
Fig. 5 Plane wave pulse at different time instant.

The plane wave pulse can be understood as plane wave fields limited by two wavefronts *W1* and *W2* as shown in Fig. 5. k indicates the incident direction. By our definition, the location of pulse when *t=0* is bounded between the following limits

$$-\frac{\tau c}{2} \le \bar{k} \cdot \bar{r} \le \frac{\tau c}{2} \tag{26}$$

That is, at *t=0*, the center of the pulse is right at the origin. Inside the two fronts, we have field illumination. Outside the fronts the field vanishes. Specifically, we have the following inequality,

$$-\frac{\tau}{2} \le t - \bar{k} \cdot \bar{r}/c \le \frac{\tau}{2} \tag{27}$$

where *t* denotes the changing variable in time and $\bar{r}$ denotes the space vector variable. At particular time instant *t=t₁* we can change (27) as

$$t_1 c - \frac{\tau c}{2} \le \bar{k} \cdot \bar{r} \le t_1 c + \frac{\tau c}{2} \tag{28}$$

The physical interpretation for (28) is that at a certain time instant t_1, a particular space location $\bar{r}$ is illuminated by the plane wave pulse if and only if it has component in the $\bar{k}$ direction falling within region [$t_1 c - \tau c/2$, $t_1 c + \tau c/2$] . With the knowledge of pulse location at *t=0*, we can find the one to one correspondence of time instant and the space location of the pulse and perform range gating in the section.

2.6 Range Gating Technique

The range gating technique is the most important aspect in the plane wave pulse scattering. It also has advantage over tapering at the grazing angle incidence, because it is feasible to restrict the length of rough surface for our studying.

Multiple scattering will create response outside the observation "window" in time domain. But they tend to be small and negligible. With the range gating technique, only a segment of the rough surface will be illuminated within a certain time interval. This segment, just like others, satisfies the same statistical distribution (Gaussian distribution, for example), which makes itself an appropriate studying object as the representation of the whole large rough surface. Besides, by carefully timing, we can let the pulse fit wholly within the segment of the interest and thus avoid the tough edge diffraction issue. Fig. 6 shows this idea.
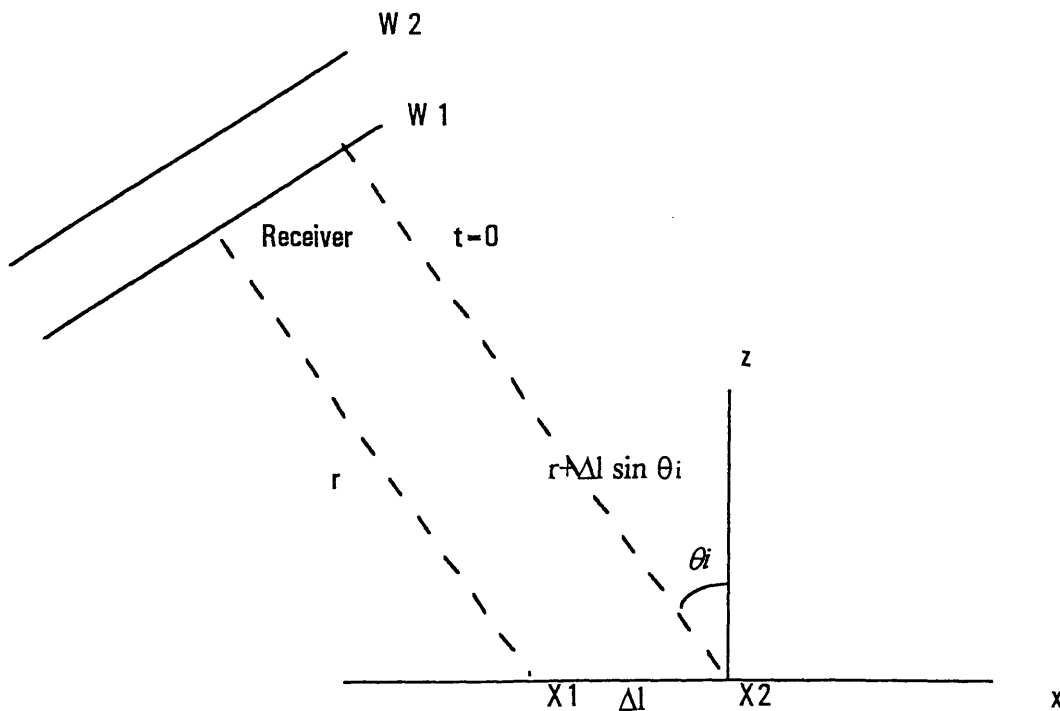
Fig. 6 Plane wave pulse incidence to a finite flat plate.

As indicated in Fig. 6, the plane wave pulse is constrained by the leading edge *W1* and the trailing edge *W2*. The incident angle is θ_i. Let segment *X1 -- X2* be our area of interest. Also let the distance between receiver and point *X1* be r, then the distance between the receiver and point *X2* would be $(r + \Delta l \sin\theta_i)/c$. At first look, the time interval of returned scattered field from this segment starts when wavefront *W1* hits *X1* and returns to receiver and ends when wavefront *W2* hits *X2* and returns to receiver. Therefore, the time interval is from *2r/c* to $2(r + \Delta l \sin\theta_i)/c + \tau$ where τ is the pulse duration and c is the speed of the light. However, this scheme will include the scattering of the rough surface outside our segment. Thus, to obtain the scattering completely due to the specified segment, our starting time instant t_1 is when wavefront *W2* hits *X1* and returns to the receiver. The stopping time instant t_2 is when wavefront *W1* hits *X2* and returns to the receiver. Therefore, we have

$$t_1 = 2\,r/c + \tau, \quad t_2 = 2\,(r + \Delta l \sin\theta_i)/c \qquad (29)$$

Notice that this plane wave pulse travels along the plate continuously and the receiver will get returns from different location of the plate. To discriminate the scattered field from the selected surface segment, we can time gate at the receiver, using this interval indicated before, to make sure only the scattered field from the segment of interest is received.

The resolution of the time gating technique is the basis for our decision of the minimum plate size, which will be discussed later. To find this resolution, let's define the following parameters in Fig. 6.

t=0   when *W1* hits the receiver

$t_{11} = 2r/c$ the time needed for *W1* to hit *X1* and to return to receiver

$t_{12} = 2(r + \Delta l \sin \theta)/c$ the time needed for *W1* to hit *X2* and to return to receiver

$t_{21} = 2r/c + \tau$ the time needed for *W2* to hit *X1* and to return to receiver

$t_{22} = 2(r + \Delta l \sin \theta)/c + \tau$ the time needed for *W2* to hit *X2* and to return to receiver

The receiver cannot tell the scattered field due to *W1* hitting *X2* or *W2* hitting *X1* if

$$\tau = 2 \Delta l \sin \theta /c \Rightarrow \Delta l = \tau c/2\sin \theta$$

where Δl is the resolution along the *x* direction. From the above equation, we find that as the angle approaches grazing, i.e. θ increases, the resolution also increases. Also, we notice that resolution increases as τ decreases. Since maintaining a significant signal to noise ratio requires keeping the pulse length at certain level, we are facing a contradiction. In the same time, we know that the bandwidth of the signal is inversely proportional to the pulse length. To obtain a good RCS approximation, we need a small bandwidth, i.e. large pulse length. This constructs another contradiction. Therefore, we need to find a compromise, as will be discussed in Chapter 4.

A question is raised when our algorithm is going to be implemented. How long the segment along the direction of incidence should we choose to do the time (or range) gating? We first express the minimum plate size in terms of pulse length τ.

Fig. 7 shows the configuration. The incident wave is incoming at angle θ. 0 denotes the origin and let's suppose when $t=0$, the leading edge of the pulse just hits the origin. *D1, D2, D3* and *D4* denotes different locations of the plate, respectively

When the leading edge hits *D1* and *D2* and gets back, the time instants are given by

$$t_{d1} = 2\,D1\,sin\,\theta_i/c, \quad t_{d2} = 2\,D2\,sin\,\theta_i/c \tag{30}$$

Since when the leading edge hits *D2*, the pulse should be completely inside the region defined by *D1* and *D2* , we have

$$t_{d2} \geq t_{d1} + \tau \tag{31}$$

Similarly, the time instants for the first wavefront to hit *D3* and *D4* and get back are

$$t_{d3} = 2\,D3\,sin\,\theta_i/c, \quad t_{d4} = 2\,D4\,sin\,\theta_i/c \tag{32}$$
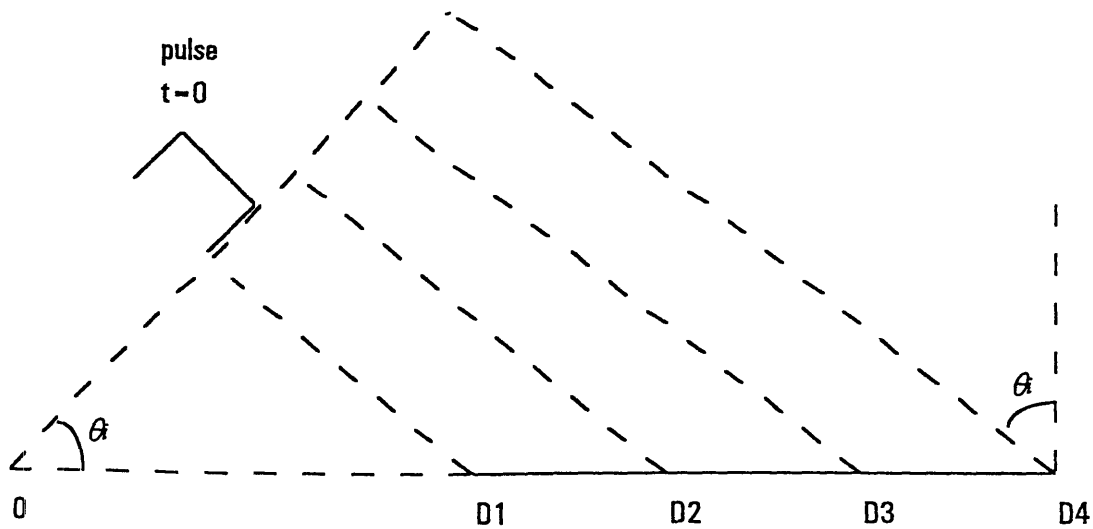
Fig. 7 Minimum plate size configuration.

When pulse completely fits inside region defined by *D3* and *D4*, we have again

$$t_{d4} \geq t_{d3} + \tau \tag{33}$$

When *D2* and *D3* overlaps, i.e., when $t_{d2} = t_{d3}$, we have

$$t_{d4} \geq t_{d2} + \tau \geq t_{d1} + 2\tau \tag{34}$$

Substituting (30) and (32) into (34) and rearranging the inequality, we obtain

$$2(D4 - D1)\sin\theta_i/c \geq 2\tau \tag{35}$$

So the constraint on the plate size *D4-D1* is given as

$$D4 - D1 \geq \tau c / \sin\theta_i \tag{36}$$

Therefore the minimum plate size is $\tau c / \sin\theta_i$.

2.7 Calculation of RCS

A general rough surface has its random roughness distribution along both x and y directions. Here we only consider the 1D rough surface, i.e., a surface that has height variation in only one dimension, say along the x axis. The RCS is defined to be

$$\sigma = \frac{4\pi r^2}{A} \frac{|E_s|^2}{|E_i|^2}$$

where A is the projected area of the rough surface plate and r is the distance between the observation point and the origin, which is much larger than the plate size.

Our numerical simulation of RCS is based upon the time domain response. Following the definition, the RCS should be calculated by

$$\sigma_t = 2\pi \frac{r}{\Delta a} \frac{\int_{t_1}^{t_2} dt\, |E_s|^2}{\int_{-\tau/2}^{\tau/2} dt\, |E_i|^2} \tag{37}$$

where E_s is the calculated scattered field in time and E_i is the incident field in time. t_1 and t_2 are the starting and ending time instants as discussed in the previous section. r is the distance between the receiver and the origin and Δa is the effective length of illuminated region and is equal to the projection length of the rough surface on the x axis subtracted by the effective pulse length.

As discussed in section 2.5, at $t=0$, the center of the pulse is located at the origin. To determine the integration period, we refer to Fig. 8.
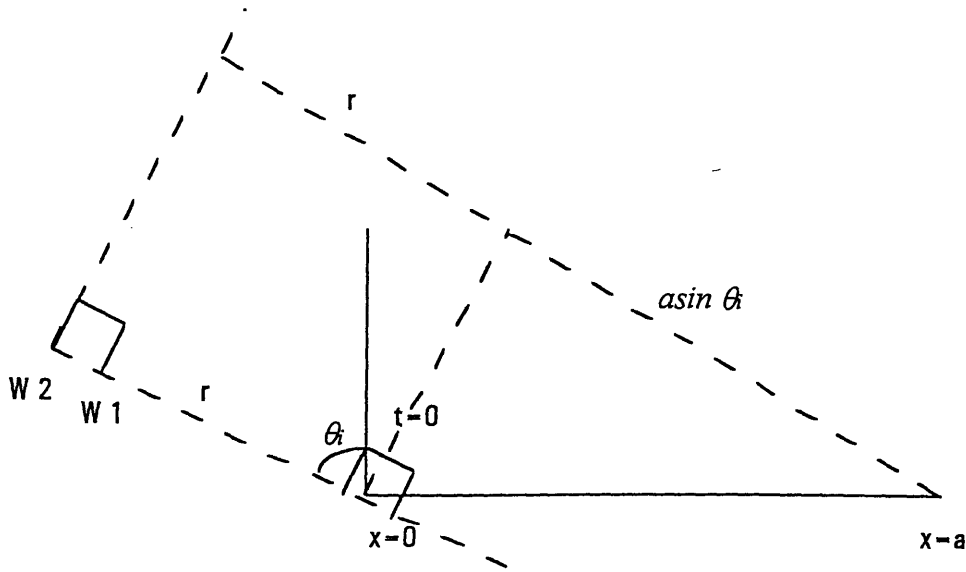
Fig. 8 RCS integration interval determination.

The beginning time instant t_1 for integral in the numerator is defined as when the trailing edge $W2$ hits the origin at time $\tau/2$ instant and travels back to the receiver with a distance measuring from the leading edge location, so we have

$$t_1 = r/c + 3\tau/2$$

The ending time instant t_2 is defined as when leading edge hits the end of the plate at time instant $a \sin \theta_i/c - \tau/$ and gets back to the receiver at time instant $(r+a \sin \theta_i)/c + a \sin \theta_i/c - \tau/$. Again we have

$$t_2 = r/c + 2a \sin \theta_i/c - \tau/2$$

Notice that the duration of observation or the time gate is

$$t_2 - t_1 = 2(a \sin \theta_i - \tau)$$

which is proportional to the effective length of illumination Δa.

In summary, our methodology is to obtain the scattering results from different rough surface realizations using MOM. At each realization, we calculate the frequency domain return and synthesize the time signal. Then the RCS is computed using (37), averaged over different realizations and compared with the results obtained from analytic approximation techniques.

Chapter 3 Pulse Compression for 1D Rough Surface Scattering

The pulse compression technique makes use of the Fourier synthesis procedure to assemble the pulse from frequency components. We shall now review possible pulse waveforms. Each of them has different bandwidth and sidelobe pattern.

3.1 Characteristics of Different Types of Pulses

As discussed before, our approach to get the time scattering due to the incident pulse is to synthesize the scattering at different frequency components. We need to select a proper pulse form that has modest requirement on both the mainlobe bandwidth and sidelobe level. This provides the motivation for us to study the pulses commonly used in signal processing, with the comparison of the mainlobe bandwidth and the peak sidelobe value.

3.1.1 Rectangular Pulse

Rectangular pulse is the most commonly used pulse form in signal processing, given as

$$p_r(t) = u(t+\tau/2) - u(t-\tau/2) \tag{38}$$

where $u(\ )$ is the step function and τ is the pulse length. Its Fourier transform is

$$P_r(\omega) = \int_{-\infty}^{+\infty} p_r(t)\, e^{i\omega t}\, dt = \int_{-\tau/2}^{+\tau/2} e^{i\omega t}\, dt = \frac{2\sin(\omega\,\tau/2)}{\omega} \tag{39}$$

where ω is the radian frequency. The time and spectrum is plotted in Fig. 9.

To find the mainlobe bandwidth, we set

$$P_r(\omega) = \frac{2 \sin (\omega \, \tau/2)}{\omega} = 0 \tag{40}$$

Therefore, we have

$$\omega \, \tau/2 = n\pi \tag{41}$$

When $n=0$, we have $\omega = 0$, where spectrum reaches its maximum 2. The first zeros of (40) happen when $n = \pm 1$, so the mainlobe bandwidth is given by

$$BW_r = [\pi - (-\pi)] \, 2/\tau = 4\pi/\tau \tag{42}$$
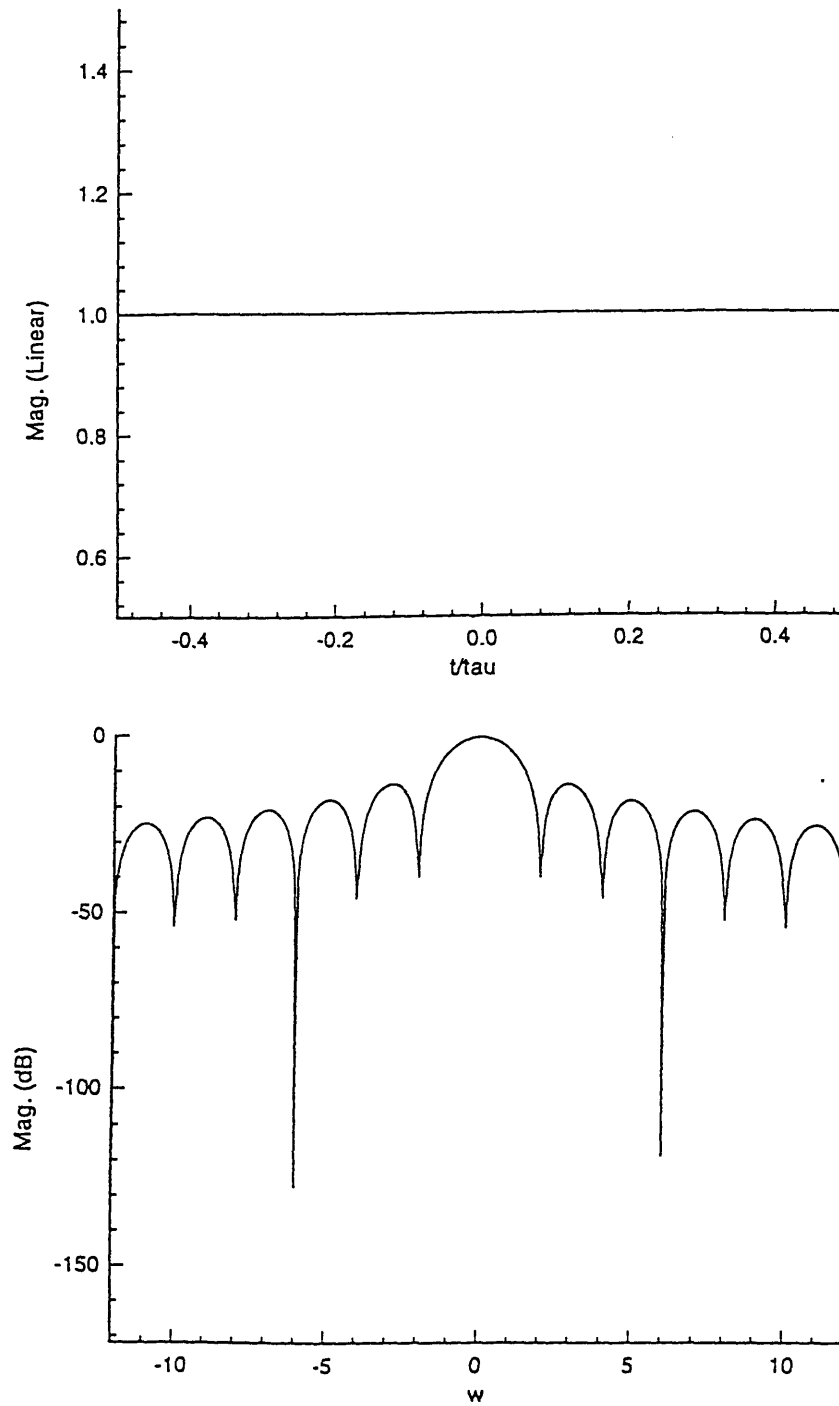
Fig. 9 Rectangular pulse in time and frequency domains.

To obtain the peak sidelobe value, let's take the derivative of (39) with respect to ω and have

$$\frac{d\,P_r}{d\,\omega} = \frac{\omega\,\tau\cos(\omega\,\tau/2) - 2\,sin\,(\omega\,\tau/2)}{\omega^2} \tag{43}$$

By setting (43) to be zero, we can find the local extrema satisfies equation (44)

$$\omega = \frac{2}{\tau}\,tan(\omega\,\tau/2) \tag{44}$$

Solving (44) by graphics, we find that the first peak sidelobe value approximately happens at $\omega = 4.918\pi/\tau$. So, the peak sidelobe value scaled according to the mainlobe peak value is given as

$$|P_{rsbmax}| \approx sin\,(4.918\,\pi/\tau \cdot \tau/2)/\,4.918\,\pi/\tau \approx 0.0642\,\tau \tag{45}$$

3.1.2 Bartlett (triangular) Pulse

The triangular pulse is expressed as

$$p_{tr}\,(t) = 1 - 2t/\tau \ \ for \ \ 0 \le t \ \le \ \tau/2 \tag{46a}$$

$$p_{tr}\,(t) = 1 + 2t/\tau \ \ for \ \ -\tau/2 \le t \le 0 \tag{46b}$$

$$p_{tr}\,(t) = 0, \qquad otherwise \tag{46c}$$

The triangular pulse can be expressed as the convolution of two rectangular pulses

$$P_{tr}(t) = \frac{2}{\tau} \left[p_{rc}(\tau/2) \otimes p_{rc}(\tau/2) \right] \qquad (47)$$

where

$$p_{rc}(\tau/2) = u(t+\tau/4) - u(t-\tau/4)$$

From the convolution theorem, the Fourier transform of (47) can be easily obtained as

$$P_{tr}(\omega) = \frac{8 \sin^2(\omega \, \tau/4)}{\tau \, \omega^2} \qquad (48)$$

The time and frequency plot for the Bartlett pulse is shown in Fig. 10.

The peak mainlobe value is increased to 4 and the mainlobe bandwidth is given as

$$BW_{tr} = [\pi - (-\pi)] 4/\tau = 8\pi/\tau \qquad (49)$$

Taking the derivative of (48) with respect to ω , we have

$$\frac{d P_{tr}}{d \omega} = \frac{2\omega \, \tau \sin(\omega \, \tau/4) \cos(\omega \, \tau/4) - 8 \sin^2(\omega \, \tau/4)}{\omega^3} \qquad (50)$$

By setting (50) to be zero and using similar way as in (44), we can find that the first peak sidelobe value happens at $\omega = 4.918 \, \pi/\tau/2 = 9.836 \, \pi/\tau$. The peak sidelobe value normalize to the peak mainlobe value is

$$|P_{trsbmax}| \approx 0.00103 \, \tau^2 \qquad (51)$$
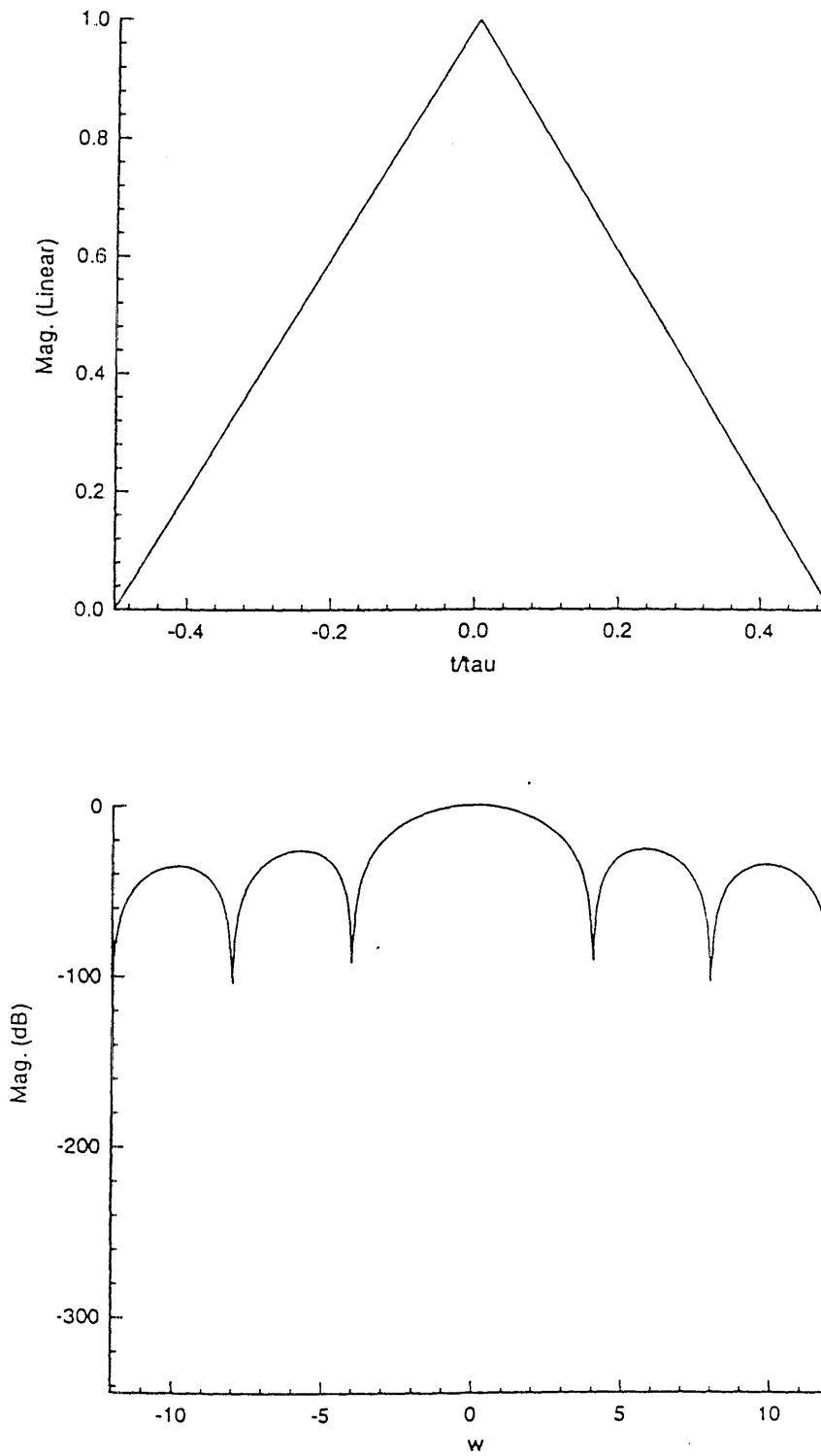
Fig. 10 Bartlett pulse in time and frequency domains.

Since $\tau \ll 1$, for the same pulse length τ, the peak sidelobe value of the Bartlett pulse is much smaller than that of the rectangular pulse at the expense of doubling its mainlobe bandwidth.

3.1.3 Hanning, Hamming and Blackman Pulses

The general expression for Hanning, Hamming and Blackman pulses can be expressed as

$$p(t) = [\, a_1 + a_2 \cos (\frac{2\pi t}{\tau}) + a_3 \cos (\frac{4\pi t}{\tau}) \,] \, [u(t+\tau/2) - u(t-\tau/2)] \tag{52}$$

where a , a and a have the corresponding values for three pulses as shown in Table 1.

Table 1 Coefficients for Hanning, Hamming and Blackman Pulses

The Fourier transform of (52) can be obtained in two steps.

First, let

$$p_1(t) = [\, a_1 + a_2 \, cos \, (\frac{2\pi t}{\tau}) + a_3 \, cos \, (\frac{4\pi t}{\tau})\,] \tag{53}$$

Its Fourier transform is given by

$$P_1(\omega) = 2a_1 \pi \delta(\omega) + a_2 \pi [\delta(\omega + 2\pi/\tau) + \delta(\omega - 2\pi/\tau)] + a_3 \pi [\delta(\omega + 4\pi/\tau) + \delta(\omega - 4\pi/\tau)] \tag{54}$$

So, by using (38) and (39), we have

$$p(t) = p_1(t) \, p_r(t) \tag{55}$$

and

$$P(\omega) = \frac{1}{2\pi} P_1(\omega) \otimes P_r(\omega) \tag{56}$$

$$= \frac{1}{2}\{2a_1 \delta(\omega) + a_2[\delta(\omega + 2\pi/\tau) + \delta(\omega - 2\pi/\tau)] +$$

$$a_3[\delta(\omega + 4\pi/\tau) + \delta(\omega - 4\pi/\tau)]\} \otimes \frac{2 \, sin \, (\omega \, \tau/2)}{\omega}$$

$$= 2a_1 \frac{sin(\omega\tau/2)}{\omega} + a_2 \{\frac{sin[(\omega + 2\pi/\tau)\tau/2]}{\omega + 2\pi/\tau} + \frac{sin[(\omega - 2\pi/\tau)\tau/2]}{\omega - 2\pi/\tau}\}$$

$$+ a_3 \{\frac{sin[(\omega + 4\pi/\tau)\tau/2]}{\omega + 4\pi/\tau} + \frac{sin[(\omega - 4\pi/\tau)\tau/2]}{\omega - 4\pi/\tau}\}$$

For Blackman pulse a_3 is not zero, so the mainlobe bandwidth is

$$BW_{bl} = [3\pi - (-3\pi)] \, 2/\tau = 12\pi/\tau \qquad\qquad (57)$$

For Hamming and Hanning, a_3 is zero, so the mainlobe bandwidth is

$$BW_{han} = BW_{ham} = [2\pi - (-2\pi)] \, 2/\tau = 8\pi/\tau \qquad\qquad (58)$$

It can be computed that the peak sidelobe value of the five pulses discussed above has the following relation

$$S_{b\,rcmax} > S_{b\,trmax} > S_{b\,hanmax} > S_{b\,hammax} > S_{b\,blkmax} \qquad\qquad (59)$$

Their mainlobe bandwidth has the following relation

$$BW_{rc} < BW_{tr} = BW_{han} = BW_{ham} < BW_{blc} \qquad\qquad (60)$$

We plot out the time and frequency distributions of the three pulses in Fig. 11-13.

Blackman pulse has the smallest sidelobe value but its mainlobe bandwidth is the largest. Rectangular pulse has the smallest mainlobe bandwidth but its sidelobe level is the highest. To choose an appropriate pulse form, we need the sidelobe peak value to be as small as possible with a moderate mainlobe bandwidth. Noticing that the mainlobe
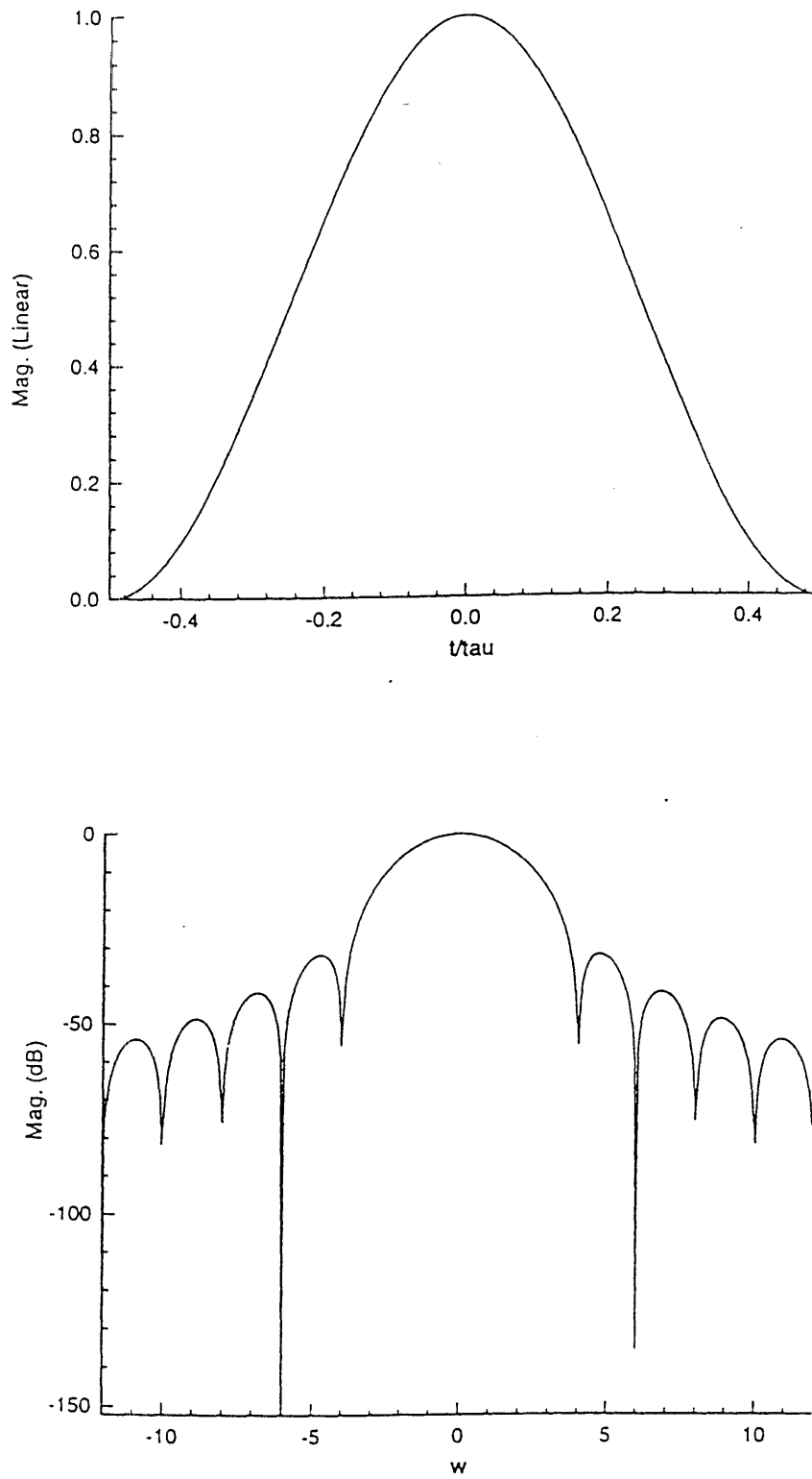
Fig. 11 Hanning pulse in time and frequency domains.
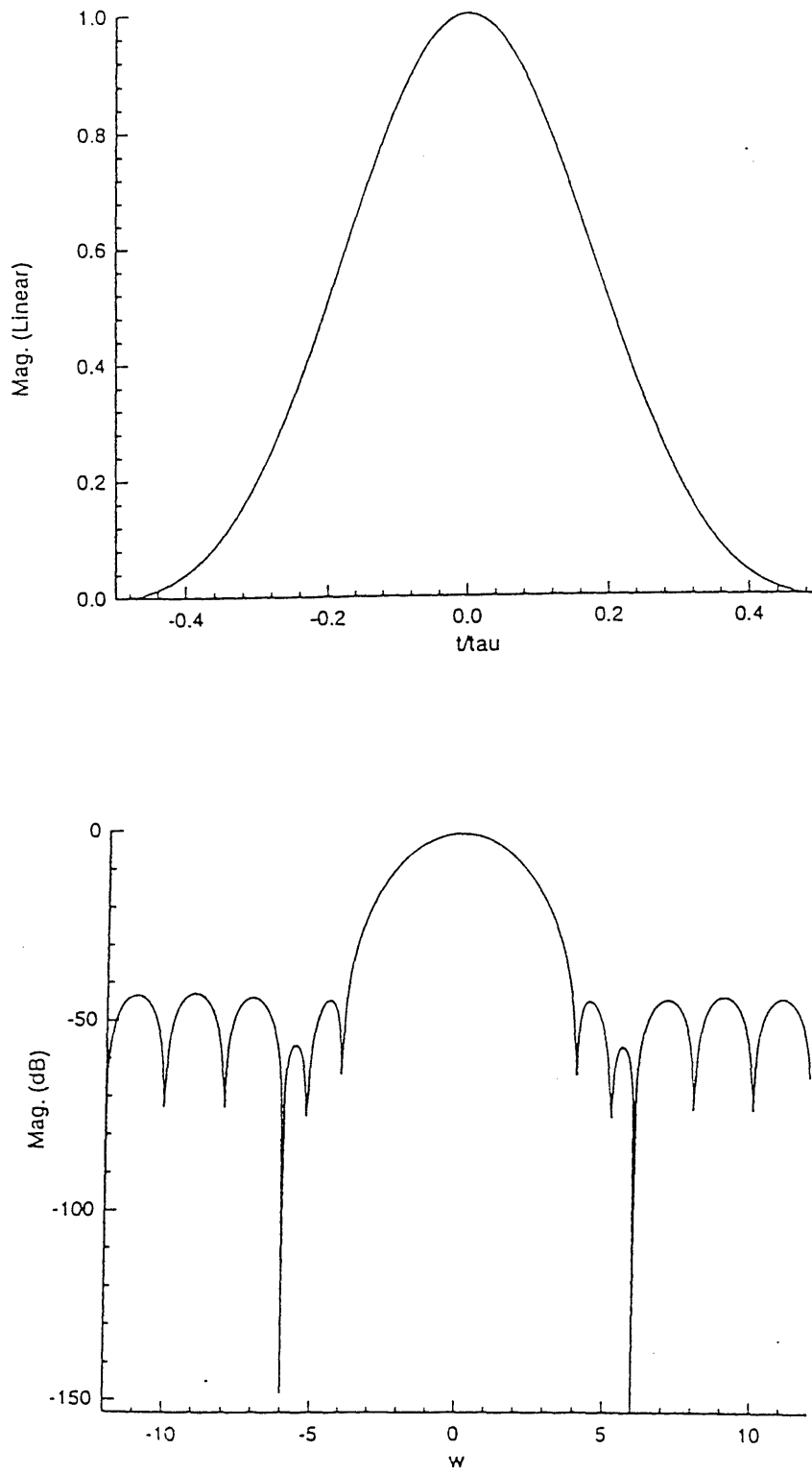
Fig. 12 Hamming pulse in time and frequency domains.
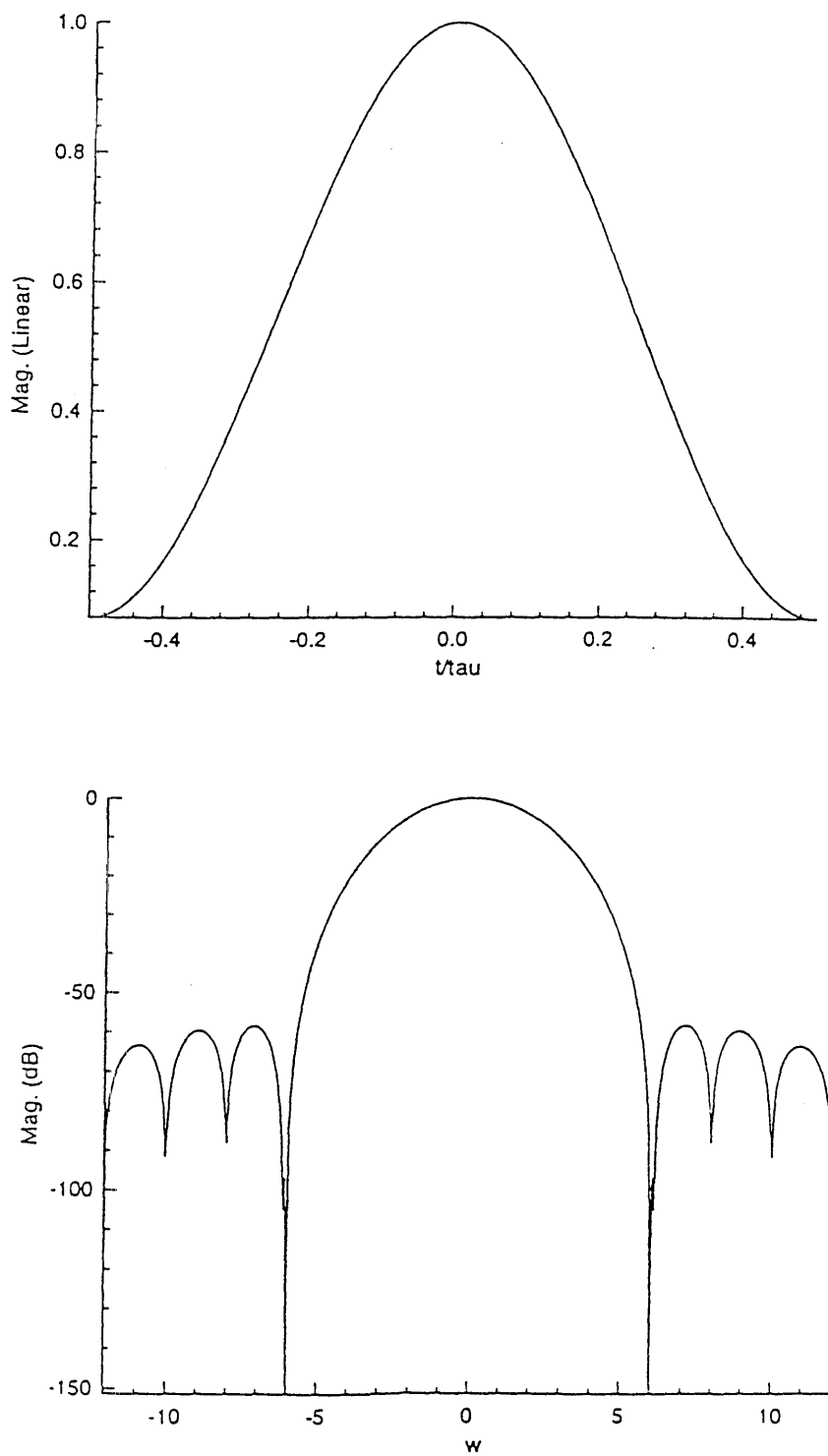
Fig. 13 Blackman pulse in time and frequency domains.

bandwidth of Bartlett, Hanning and Hamming are the same and that Hamming pulse has the lowest sidelobe level among the three, we decide to use Hamming pulse as our choice which will be discussed in later sections.

3.2   Hamming Pulse and Its Plane Wave Expression

3.2.1 Hamming Pulse

Based on the above considerations, we choose Hamming pulse as our pulse representation whose time expression is given as,

$$h_m(t) = cos\,(\omega_0 t)\,[0.54 + 0.46\,cos\,(2\pi t/\tau)\,]\,[u(t + \tau/2) - u(t - \tau/2)] \qquad (61)$$

By using (56) with the coefficients substituted for Hamming pulse, we have the Fourier transform as

$$H_m(\omega) = \frac{1}{2\pi}\,\pi\,[\delta(\omega + \omega_0) + \delta(\omega - \omega_0)] \otimes P(\omega) \qquad (62)$$

Therefore, we have

$$H_m(\omega) = 0.54 \frac{\sin\left[(\omega-\omega_0)\frac{\tau}{2}\right]}{\omega-\omega_0} + 0.54 \frac{\sin\left[(\omega+\omega_0)\frac{\tau}{2}\right]}{\omega+\omega_0} + 0.23 \frac{\sin\left[(\omega-\omega_0\frac{2\pi}{\tau})\frac{\tau}{2}\right]}{\omega-\omega_0\frac{2\pi}{\tau}} +$$

$$0.23 \frac{\sin\left[(\omega+\omega_0+\frac{2\pi}{\tau})\frac{\tau}{2}\right]}{\omega+\omega_0+\frac{2\pi}{\tau}} + 0.23 \frac{\sin\left[(\omega-\omega_0+\frac{2\pi}{\tau})\frac{\tau}{2}\right]}{\omega-\omega_0+\frac{2\pi}{\tau}} + 0.23 \frac{\sin\left[(\omega+\omega_0-\frac{2\pi}{\tau})\frac{\tau}{2}\right]}{\omega+\omega_0-\frac{2\pi}{\tau}} \qquad (63)$$

In our simulation scheme, the sidelobe contibution will be ignored. The frequency scattering component will be constrained in the mainlobe. Thus we approximate Hamming pulse as a band-limited signal.

3.2.2 Modulated Hamming Pulse Plane Wave

Eq. (61) can be modified to give the plane wave Hamming pulse expression.

$$a_m(t) = \cos(\omega_o(t - \hat{k}\cdot\bar{r}/c)) \{0.54 + 0.46 \cos[(2\pi/\tau)(t - \hat{k}\cdot\bar{r}/c)]\} \qquad (64)$$

$$[u(t - \hat{k}\cdot\bar{r}/c + \tau/2) - u(t - \hat{k}\cdot\bar{r}/c - \tau/2)]$$

Its Fourier transform can be easily obtained by finding time shift expression of Eq. (63)

$$A_m(\omega) = e^{i\,\omega \hat{k}_i \cdot \bar{r}/c} \{0.54 \frac{sin\,[(\omega-\omega_0)\frac{\tau}{2}]}{\omega-\omega_0} + 0.54 \frac{sin\,[(\omega+\omega_0)\frac{\tau}{2}]}{\omega+\omega_0} + 0.23 \frac{sin\,[(\omega-\omega_0-\frac{2\pi}{\tau})\frac{\tau}{2}]}{\omega-\omega_0-\frac{2\pi}{\tau}} +$$

$$0.23 \frac{sin\,[(\omega+\omega_0+\frac{2\pi}{\tau})\frac{\tau}{2}]}{\omega+\omega_0+\frac{2\pi}{\tau}} + 0.23 \frac{sin\,[(\omega-\omega_0+\frac{2\pi}{\tau})\frac{\tau}{2}]}{\omega-\omega_0+\frac{2\pi}{\tau}} + 0.23 \frac{sin\,[(\omega+\omega_0-\frac{2\pi}{\tau})\frac{\tau}{2}]}{\omega+\omega_0-\frac{2\pi}{\tau}} \} \qquad (65)$$

where $\hat{k}$ is the unit vector for wave incident direction, $\bar{r}$ is the space vector started from the origin and c is the speed of the light.

3.3 Frequency Decomposition and Time Return Synthesis

In order to run the MOM scattering cimputation program in frequency domain, we first decompose the incident pulse into different frequency components. After that, scattering return is synthesized into time expression for future application.

3.3.1 Frequency Decomposition

The frequency decomposition is equivalent to the frequency sampling. For the incident signal, we know the frequency spectrum exactly. Thus, the sampling can be performed easily. For the scattering signal, however, we know nothing about its whole frequency spectrum except the individual scattering return for the sampled input signal using the MOM program. Neither do we know the scattering signal in time. Therefore, the question is how many frequency components we should choose so that the scattering signal in time can be constructed accurately without aliasing.

We know nothing about the scattering time signal except for its time duration, which can be obtained from the plate size. What we also know is that the scattering frequency signal has a bandwidth equal to the mainlobe width of the input signal. This knowledge bout the scattered signal together with our sampled scattering return can help us construct time signal eventually.

Suppose we have a signal whose time and frequency duration are known. As indicated in Fig.14 (a) and (b).   The sampling in frequency domain corresponds to the repetition of the time signal as shown in   Fig. 14 (c). This can be expressed in the following equations.

Suppose we have a signal $S(\omega)$ and sample it in the frequency domain as shown in Eq. (66).

$$\hat{S}(\omega) = S(\omega) \sum_{n=-\infty}^{\infty} \delta(\omega - n\, \Delta\omega) \qquad (66)$$

where δ is the impulse function and $\Delta\omega$ is the sampling interval. This sampling procedure is equivalent to the time signal convolution as given in Eq. (67).

s(t)

shape unknown

-T/2   T/2   t

(a)

S(w)

shape unknown

-4 π / τ   4 π / τ   w

— — samples known from simulation

(b)

s(t)

shape unknown

- 2π/Δω   -T/2   T/2   2π/Δω   t

(c)
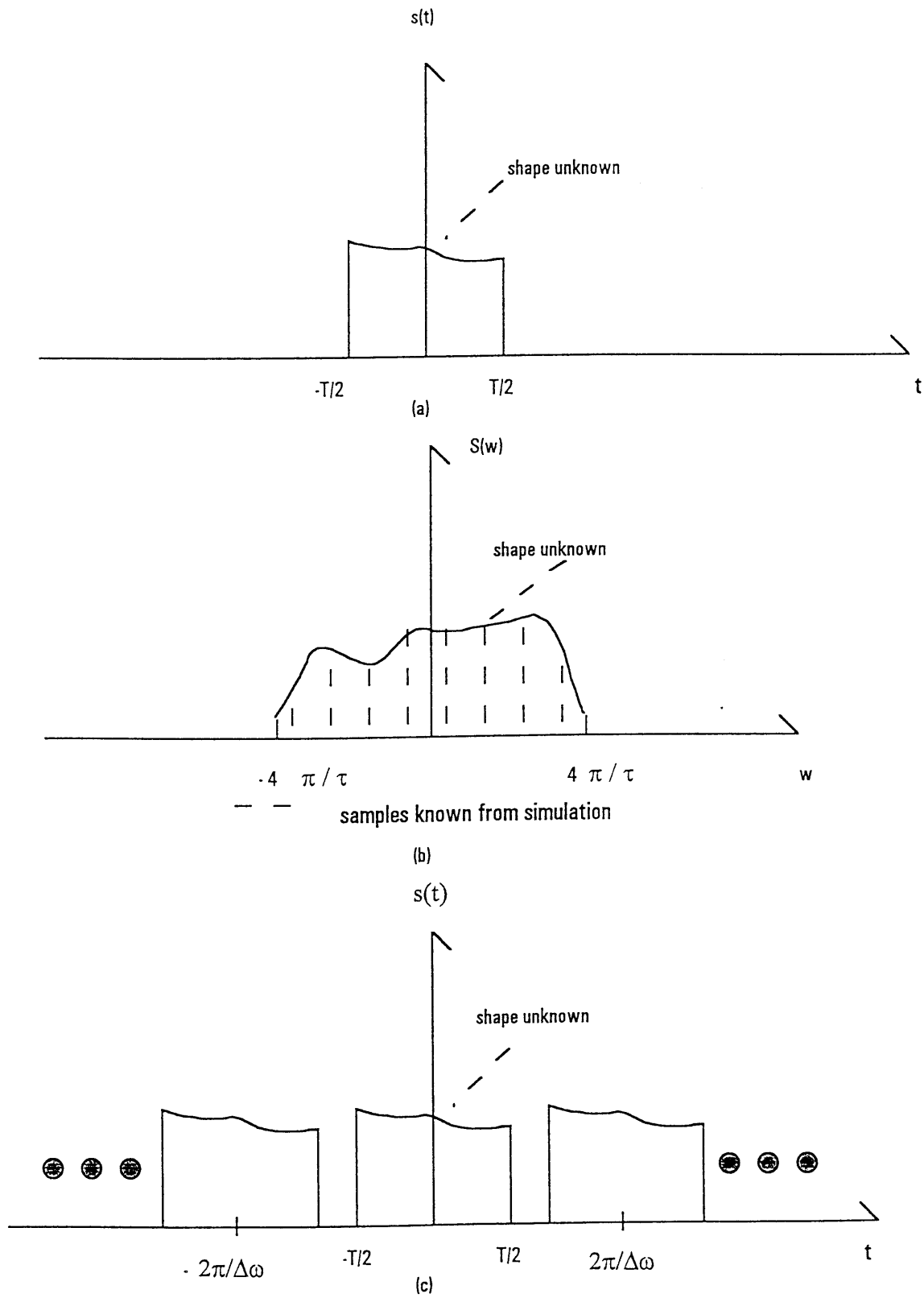
Fig. 14 Sampling in frequency domain. (a) -- time signal, (b) -- frequency

domain sampling and (c) -- Time Repetition

$$\hat{s}(t) = s(t) \otimes \frac{1}{\Delta\omega} \sum_{k=-\infty}^{\infty} \delta(t - \frac{2\pi}{\Delta\omega}k) = \frac{1}{\Delta\omega} \sum_{k=-\infty}^{\infty} s(t - \frac{2\pi}{\Delta\omega}k) \tag{67}$$

As one can note in Fig. 14, the recovered time signal is actually the repetitive version of $s(t)$, with a magnitude scale factor of $\frac{1}{\Delta\omega}$. To avoid aliasing, the following condition must be met.

$$T \le \frac{2\pi}{\Delta\omega} \Rightarrow \Delta\omega \le \frac{2\pi}{T} \tag{68}$$

Therefore the maximum sampling interval $\Delta\omega$ is $\frac{2\pi}{T}$. The actual frequency interval is much smaller than the maximum in order to get an accurate time resynthesis.

To reduce the amount of frequency component computation, it is necessary to utilize the symmetric property of the scattered signal. From Eq. (65), it can be easily proved that

$$A_m(-\omega) = A_m^*(\omega) \tag{69}$$

That is, for the incident wave A, the negative frequency component is the complex conjugate of the its positive correspondent. We next prove that the scattered field has the same symmetric property. The surface current can be expressed as

$$\bar{J}(\bar{r},\omega) = \bar{V}(\bar{r}) A_m(\omega) \tag{70}$$

Where $\bar{V}$ is a real function depending on the space vector $\bar{r}$. We can have

$$\bar{J}(r,-\omega) = \bar{J}^*(r,\omega)$$ (71)

Thus the vector potential given by

$$\bar{A}(\bar{r},\omega) = \frac{1}{4\pi} \int_C dr \bar{J}(\bar{r}',\omega) e^{-i\frac{\omega}{c}\left|\bar{r}-\bar{r}'\right|} / \left|\bar{r}-\bar{r}'\right|$$ (72)

should satisfy the symmetric property

$$\bar{A}(\bar{r},-\omega) = \frac{1}{4\pi} \int_C dr \bar{J}(\bar{r}',-\omega) e^{i\frac{\omega}{c}\left|\bar{r}-\bar{r}'\right|} / \left|\bar{r}-\bar{r}'\right| = \frac{1}{4\pi} \int_C dr \bar{J}^*(\bar{r}',\omega) e^{i\frac{\omega}{c}\left|\bar{r}-\bar{r}'\right|} / \left|\bar{r}-\bar{r}'\right| = \bar{A}^*(\bar{r},\omega)$$ (73)

Furthermore, a physical electric and magnetic field should also have the property

$$\bar{H}(r,-\omega) = \bar{H}^*(r,\omega) \quad and \quad \bar{E}(\bar{r},-\omega) = \bar{E}^*(\bar{r},\omega)$$ (74)

From previous discussion we know that the frequency components are concentrated in two bands with one around ω and the other around $-\omega$. Therefore, by computing the positive frequency components we can deduce the scattering at the correspondent negative frequency component. This approach will reduce the computational effort by half.

Another consideration is the carrier frequency ω . Fortunately, due to the characteristics of Hamming pulse, our scattered signal is assumed to be bandlimited. For the ease of further processing the time signal, we would like to get rid of the carrier frequency and get the envelope of the scattered signal. This algorithm is shown in Fig. 15 . Eq. (75), (76) give the algebra expression.
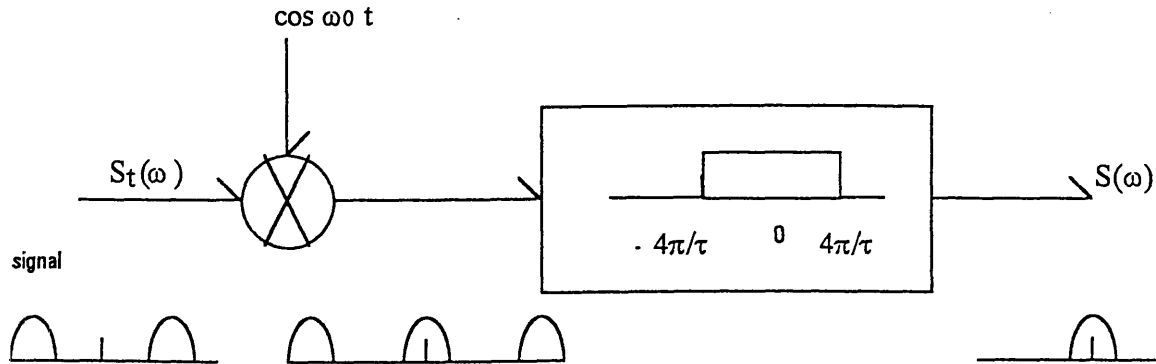
Fig. 15 Processing block to obtain the envelope of the scattered

signal.

Suppose the scattered signal is given by

$$s_O(t) = \frac{1}{2\pi} \int_{-\infty}^{\infty} S_O(\omega) e^{-i\omega t} d\omega \qquad (75)$$

where $s_O(t)$ is the scattered time signal with carrier frequency ω_O. The Fourier transform of multiplication of $s_O(t)$ and $\cos\omega_O t$ is given by

$$S_f(\omega) = 0.5 \, [S_O(\omega - \omega_o) + S_O(\omega + \omega_o)] \qquad (76)$$

The multiplication of $s_f(t)$ and $\cos\omega_O t$ will give the Fourier transform of $0.25[S_O(\omega - 2\omega_O) + S_O(\omega) + S_O(\omega + 2\omega_O)]$. We can recover $S_O(\omega)$ using low pass filter.

3.3.2 Fourier Synthesis of Time Domain Data

The time resynthesis is simply the inverse Fourier transform given by

$$s_O(t) = \frac{1}{2\pi} \int_{-\infty}^{\infty} d\omega \, S_O(\omega) \, e^{-i\omega t} = \frac{1}{2\pi} \sum_{\omega_i = -4\pi/\tau}^{4\pi/\tau} S_O(\omega_i) \, e^{-i\omega_i t} \Delta\omega \qquad (77)$$

Eq.(77) is obtained due to the fact that the input has limited bandwidth and thus $S_O(\omega)$ is approximately a banded signal from $-4\pi/\tau$ to $4\pi/\tau$. This approximation will lead to the recovered time signal to be periodic. Therefore, we need to extract the segment that corresponds to our calculation.

With the signal obtained, we can perform the range gating, i.e., time gating to obtain the scattering signal due to the truncated region and use it to calculate the RCS for further verification. We make use of the assumption that multiple scattering between illuminated and unilluminated segments is negligible in order to implement the range gating algorithm.

Chapter 4 Simulation

For simplicity, we focus our simulation on TE polarization. We first verify the correctness of the returned signal processing by extracting the envelope from the carrier frequency modulated signal, which is the start of the whole simulation scheme. The next step is to check the validity of the range gating scheme. To achieve this, we first proceed the simulation for the large rough surface plate, then we truncate the large plate into small plate and repeat the simulation. The synthesized time signals for the two plates are then compared. Finally, the Monte Carlo technique is used for rough surface scattering under small perturbation condition to be compared with the analytical SPM backscattering coefficient.

4.1 Basic Parameters

Our procedure is to perform the MOM calculations at different frequencies, resynthesize them into time domain and then calculate the RCS for verification.

First of all, we consider the input plane wave pulse.

Stripped of the space term and the carrier frequency, the incident pulse can be written as

$$E_i(t) = [0.54 + 0.46 \cos (2\pi t/\tau)\,] [u(\,t + \tau/2) - u(\,t - \tau/2)] \qquad (78)$$

55

Using the definition of RCS for 1D rough surface

$$\sigma_t = 2\pi \frac{r}{\Delta a} \frac{\int_{t_1}^{t_2} dt\,|E_s|^2}{\int_{-\tau/2}^{\tau/2} dt\,|E_i|^2} \tag{79}$$

The integration in the denominator of (79) can be computed as

$$\int_{-\tau/2}^{\tau/2} dt\,|E_i|^2 = \int_{-\tau/2}^{\tau/2} dt[0.54 + 0.46\,cos\,(2\pi t/\tau)\,]^2 \tag{80}$$

$$= \int_{-\tau/2}^{\tau/2} dt[0.54^2 + 0.46^2\,cos^2\,(2\pi t/\pi\,t/\tau) + 0.4968\,cos\,(2\pi t/\tau)\,]$$

$$= 0.3974\,\tau$$

The integral of the numerator is performed numerically as

$$\int_{t_1}^{t_2} dt\,|E_s|^2 = \sum_{t_i=t_1}^{t_2} |E_s(t_i)|^2\,\Delta t \tag{81}$$

So we can rewrite (79) as

$$\sigma_t = 2\pi \frac{r}{\Delta a} \frac{\sum_{t_i=t_1}^{t_2} |E_s(t_i)|^2\,\Delta t}{0.3974\,\tau} \tag{82}$$

Our test cases consist of rough surfaces of small scale variations, generally known as small-perturbation condition. The surfaces have the following properties

$$k\sigma << 1, \frac{\sigma}{l} << 1 \tag{83}$$

Under this condition, the Small Perturbation Method [16] gives an analytic expression for backscattering RCS as

$$\sigma_{hh} = 4\,k^3\,\sigma^2\,cos^4\,\theta_i\,w(2\,k\,sin\,\theta_i) \tag{84}$$

where σ is the rms surface height, $w(\,)$ is the Fourier transform of the normalized surface autocorrelation function for the one-dimensional rough surface, expressed as

$$w(k) = \int_{-\infty}^{\infty} dx\,e^{-x^2/l^2}\,e^{-i\,kx} \tag{85}$$

$$= \sqrt{\pi}\,l\,e^{-k^2 l^2/}$$

Substituting (85) into (84), we have the final form for the RCS for 1D SPM rough surface scattering

$$\sigma_{hh} = 4\,\sqrt{\pi}\,k^3\,\sigma^2\,l\,cos^4\,\theta_i\,e^{-k^2 l^2 sin^2\,\theta_i} \tag{86}$$

As we have discussed, the sidelobes of the Hamming pulse is negligible. Therefore we can constrain our computation within the mainlobe. However, the mainlobe bandwidth is inversely proportional to the pulse width. To define the Radar Cross Section in our simulation, we need to make the mainlobe bandwidth as small as possible,

simulation, we need to make the mainlobe bandwidth as small as possible, which means larger pulse width. But, we have to be careful that when pulse width becomes larger, it will require larger surface size, thus introducing difficulty for the MOM calculation.

Based on the considerations above, we define the mainlobe bandwidth to be $1/20\pi$ of the carrier frequency and obtain the pulse as following

$$8\,\pi/\,\tau = 2\pi f_0\,/\,20\pi \Rightarrow \tau = 80\,\pi\,/f_0 \approx 0.84\,\mu s,\ for\, f_0 = 300\,MHz$$

As discussed before, the minimum plate size is given by

$$a_{min} = \tau c\,/\,sin\,\theta_i$$

For example, if the lowest incident angle we are going to simulate is 50 deg., we choose our minimum rough surface plate size to be

$$a = 8.4 \times 10^{-7} \times 3 \times 10^{8}/sin\,50^{o} \approx 329 \approx 330\,\lambda_0$$

Notice that by setting the carrier frequency to be 300 MHz, the carrier wavelength λ_0 is just 1 m. The number of nodes per wavelength in the MOM is chosen to be the marginal 4. So totally, we have a minimum of 1320 points for out simulation.

To meet the small perturbation condition, we choose the rms height of the Gaussian random rough surface and the correlation length to be, respectively,

$$\sigma = 0.04\,\lambda_o,\ cl = 0.4\,\lambda_o$$

Except otherwise noted, we are going to use the above set of basic parameters for all subsequent simulations.

4.2 Scattering Signal Processing Verification

To verify the effectiveness of the time processing scheme discussed in section 3.3, we first generate, at equally distributed 21 frequency components within the mainlobe, the frequency domain return of the scattering due to a rough surface realization of $400\lambda_0$. The rms height and the correlation length are respectively $0.4\lambda_0$ and $4\lambda_0$. Then we resynthesize the time signal with and without removing the carrier frequency. As can be seen in Fig.16, the dashed line denotes the original signal without removing the carrier frequency while the solid line represents the time signal after removing the carrier frequency. We can see that the enveloped signal can fairly represent the original signal with the carrier frequency. Therefore, we can use the enveloped signal for our further comparisons.
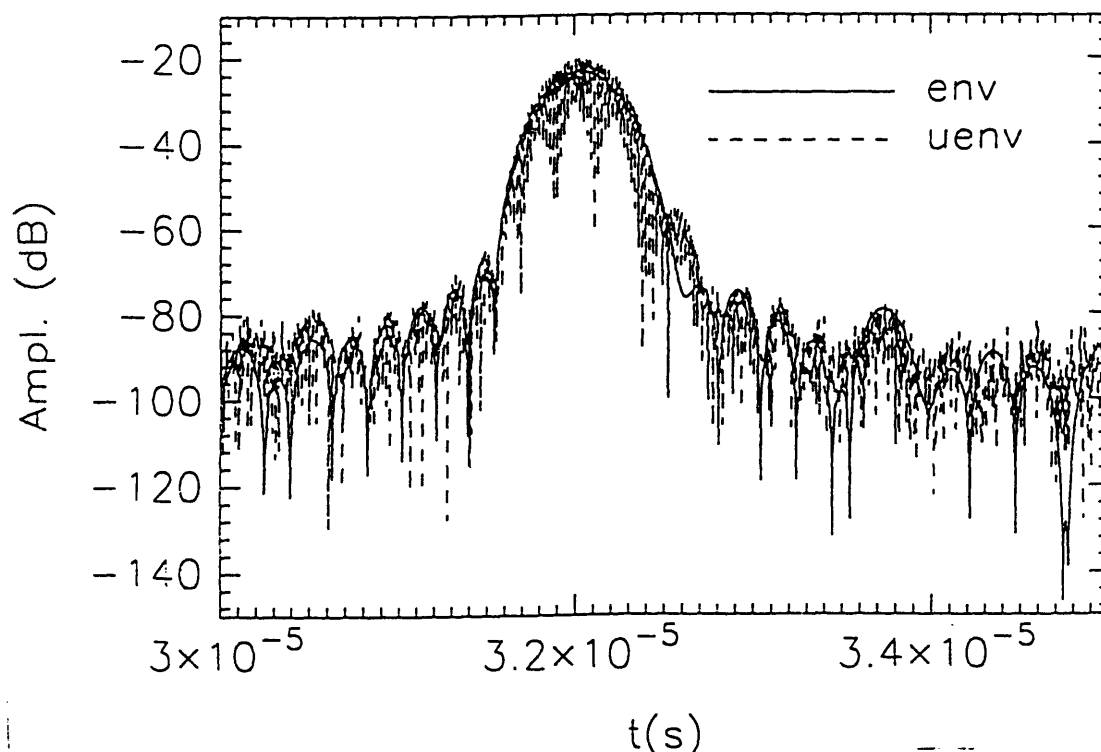
Fig. 16 Scattering Signal Processing Verification for

$\theta_i = 75^0$, $a = 400\lambda_0$, $\sigma = 0.4\lambda_0$, $cl = 4.0\lambda_0$

4.3 Range Gating Verification

The validation process can be shown in Fig. 18. The principle behind this comparison is that if at a certain time interval, only a specific segment of a large surface is illuminated, then the scattering due to this segment should be the same as that due to a similar segment in exactly the same space location without being a part of a larger surface. Here, we assume that the multiple scattering between the illuminated and unilluminated regions are negligible. So, our strategy is to extract the time scattering signal from a larger rough surface and gate it in time to find the scattering due to a specific region and then we truncate this bigger surface so that only that specific region exists in the same space location and obtain the time scattering signal and compare it with the former result.
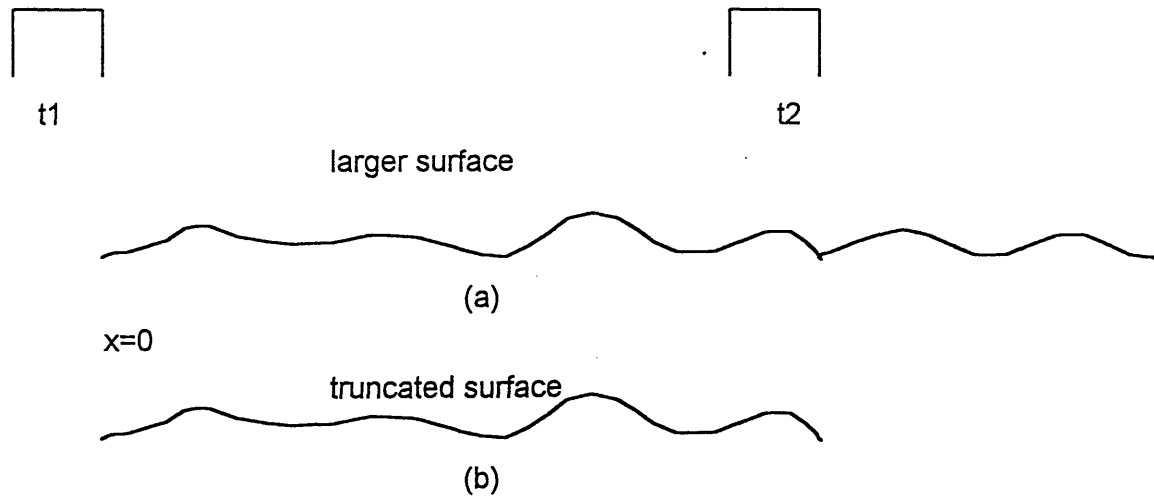
Fig. 17 Validation Scheme for Range Gating.

Based on the discussion above, we apply the simulation procedure on the bigger surface as shown in Fig. 17(a) and obtain the time return, then we truncate the bigger

surface to a smaller one in Fig. 17(b) and perform the simulation again. Finally, at different incident angles, we compare the time signal between the interval *t1* and *t2*, as shown in Fig. 18-20. Here, we denote the bigger surface size as *a1* and the truncated surface size as *a2*.
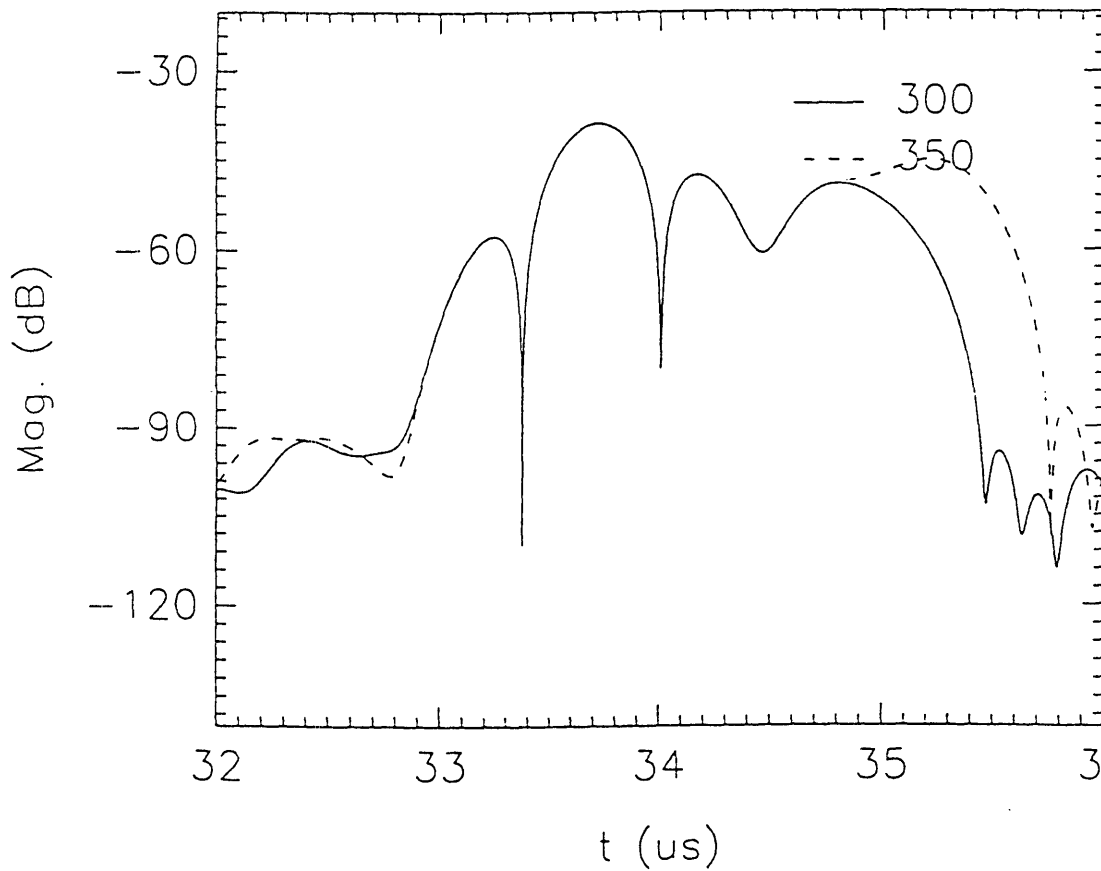
$\theta_i = 65^0$, a1 $= 350\ \lambda_0$, a2 $= 300\ \lambda_0$, $\sigma = 0.4\ \lambda_0$, cl $= 1.0\ \lambda_0$

Fig. 18 Range Gating Validation.
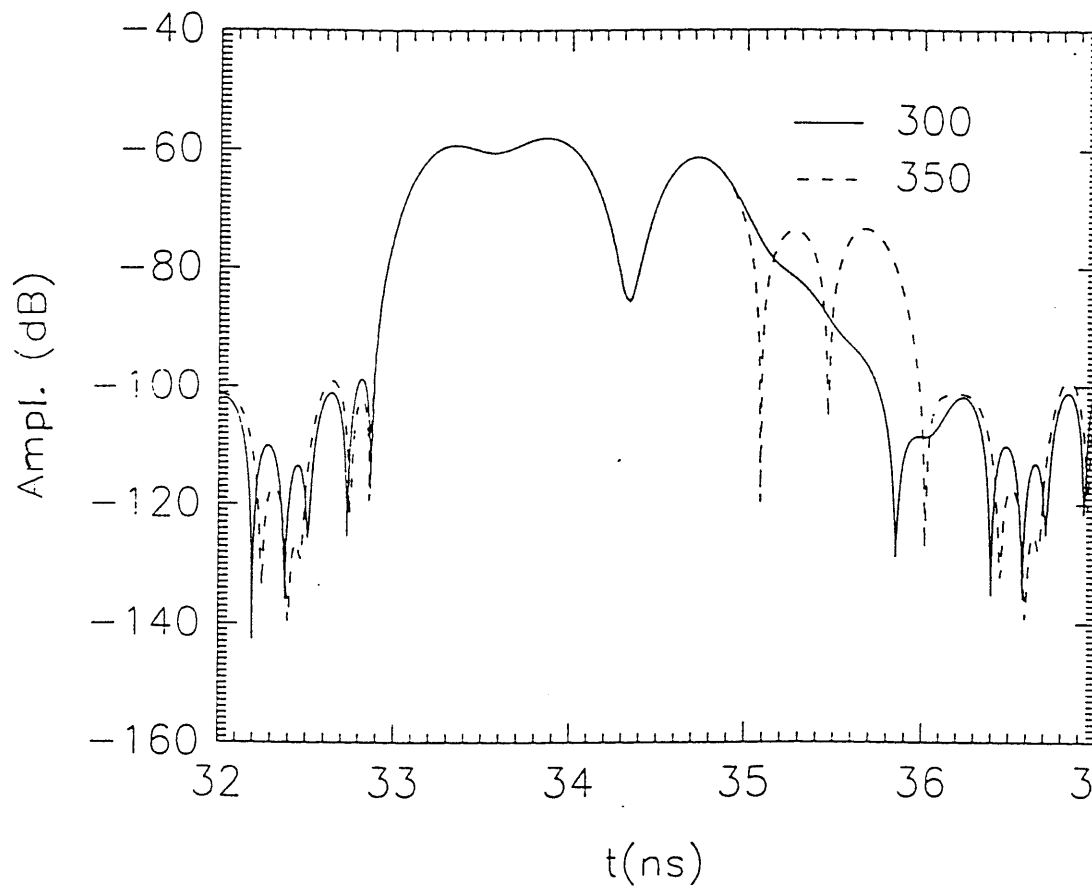
$\theta_i = 75^0$, $a1 = 350\ \lambda_0$, $a2 = 300\ \lambda_0$, $\sigma = 0.4\ \lambda_0$, $cl = 1.0\ \lambda_0$

Fig. 19 Range Gating Validation.

$\theta_i = 80^o$, a1 = 350 λ_o, a2 = 300 λ_o, σ = 0.4 λ_o, cl = 1.0 λ_o
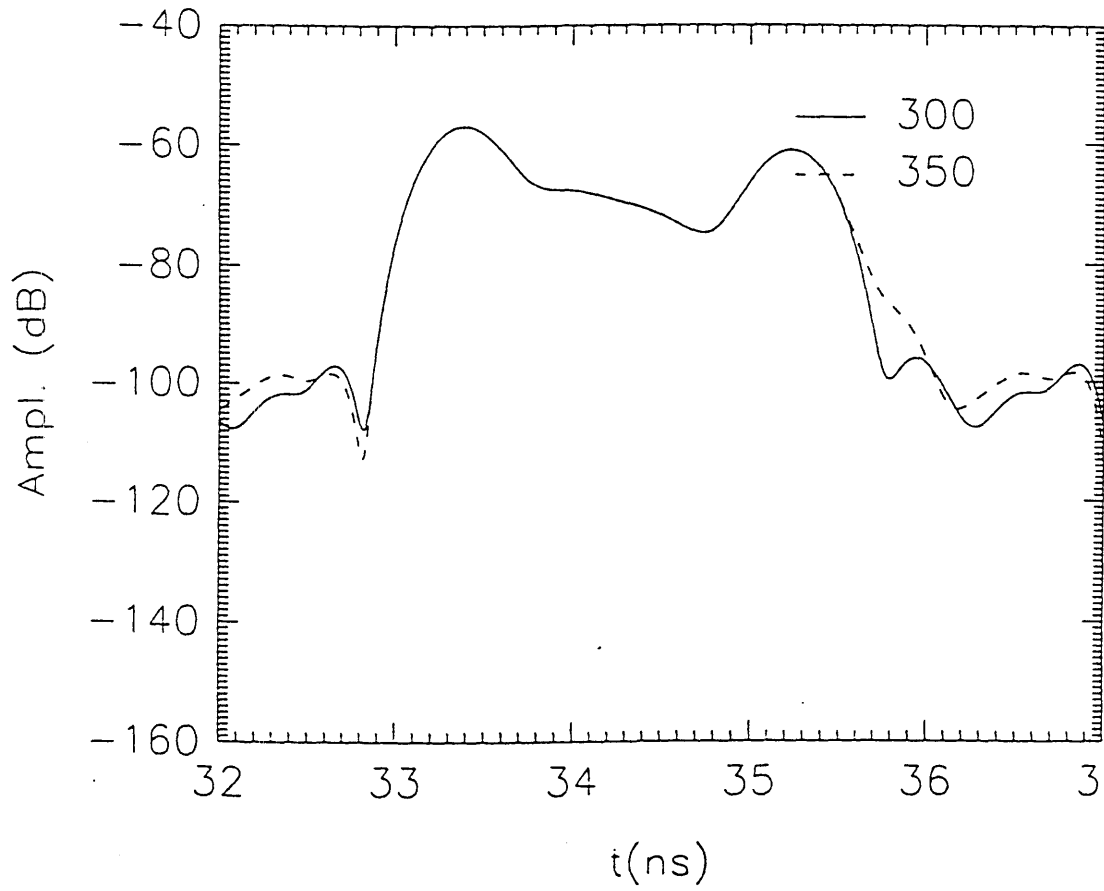
Fig. 20 Range Gating Validation.

We list the values of *t1* and *t2* in Table 2, where

$$t1 = r/c - \tau/2, \qquad t2 = r/c + 2\, a_2 \sin \theta_i /c - \tau/2$$

in which *r* denotes the receiver distance from the origin.

μ s

Table 2. Calculated Time Instants of t1 and t2.

	65 deg	75 deg	80 deg
t1 (μs)	32.91	32.91	32.91
t2 (μs)	34.73	34.85	34.88

From Fig. 18-20, we can see that between *t1* and *t2*, the scattering returns in time for both plates completely overlap each other, which verifies the validity of range gating idea.

4.4 Monte Carlo Simulation against SPM

We next proceed with the Monte Carlo simulation method for rough surface scattering under small perturbation condition. The basic procedure is shown in Fig. 21. The number of realizations is determined from results like those in Fig. 21 where the averaged scattering return converges after some number of realizations.

```
┌─────────────────┐
│   surface       │◄────────────┐
│   generation    │             │
└─────────────────┘             │
         │                      │
         ▼                      │
┌─────────────────┐             │
│  MOM frequency  │             │
│  computation    │             │
└─────────────────┘             │
         │                      │
         ▼                      │
┌─────────────────┐             │
│                 │             │
│  time synthesis │             │
│                 │             │
└─────────────────┘             │
         │                      │
         ▼                      │
┌─────────────────┐             │
│                 │             │
│ RCS calculation │             │
│                 │             │
└─────────────────┘             │
         │                      │
         ▼                      │
       ╱─────╲                  │
      ╱ enough ╲      No         │
     ╱ surfaces ╲───────────────┘
     ╲    ?     ╱
      ╲────────╱
         │ Yes
         ▼
┌─────────────────┐
│                 │
│   Averaging     │
│                 │
└─────────────────┘
```
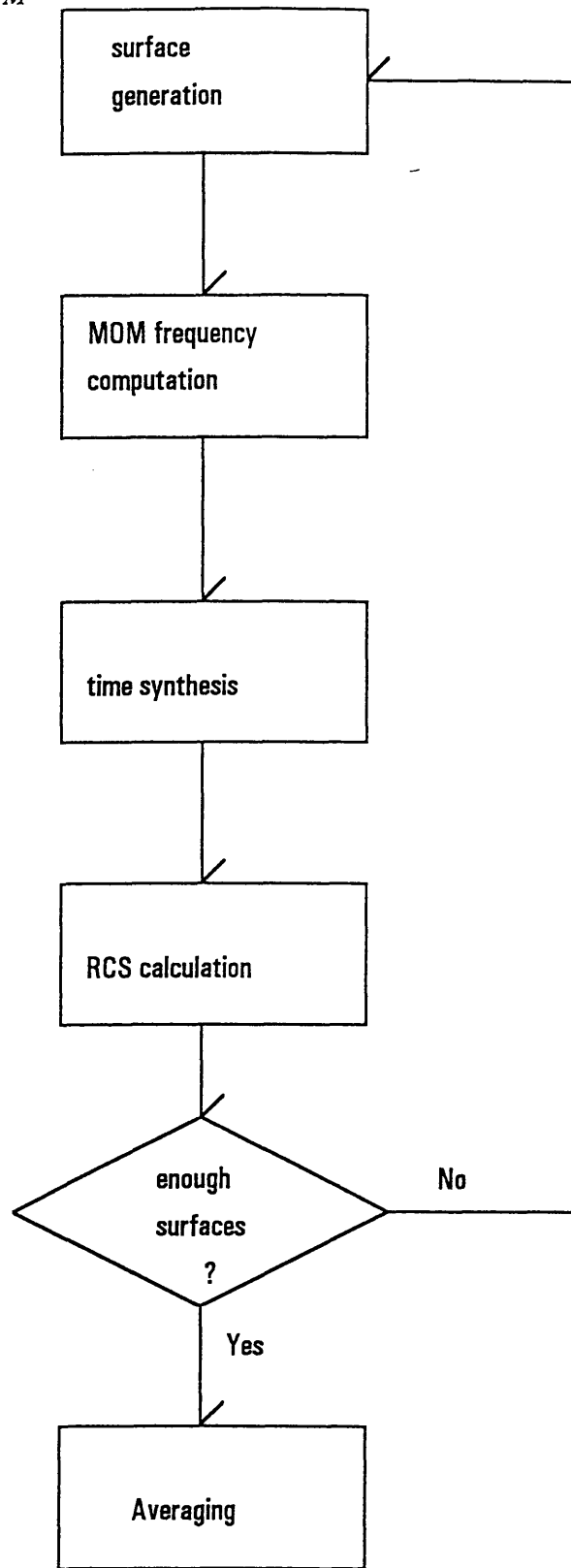
Fig. 21 Monte Carlo simulation procedure of scattering at each incident angle.

First, we have to determine the number of realizations of the rough surface for the return averaging process. In Fig. 22, we plot the averaged RCS of small perturbation rough surface with respect to number of realizations. We choose the parameters as in Table 3. It is observed that the averaging result starts to converge as the number of surfaces is bigger than or equal to 20. So we will use 20 realizations of rough surface. Again, we run at 20 evenly distributed frequencies within the Hamming pulse mainlobe and extract the time domain result.

The RCS of 1D rough surface can be calculated using (82) where the beginning and ending time instants are given by

$$t_1 = \tau/2 + (r + \tau c)/c = r/c + \frac{3}{2}\,\tau$$

$$t_2 = r/c + 2\,a\,\sin\,\theta_i/c - \tau/2$$

with a as the plate size and

$$\Delta a = a - \tau c\,/\sin\,\theta_i$$

So, with $\tau = 0.84$ μs and the number of points between t_1 and t_2, $n = 2000$, we have

$$\Delta t = (t_2 - t_1)\,/n = 0.42\,ns$$

Table 3 Parameters for simulation in Fig. 23.

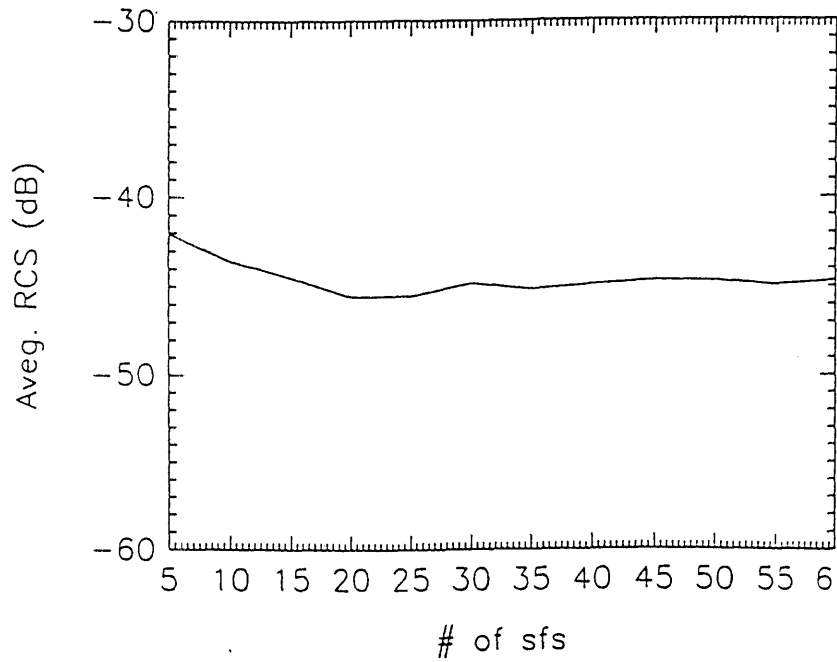| Incident Angl	Plate Size	# of Points/Wavelength
75 deg	300 λ_0	4
Rms Height	Corr. Length	# of Realizations
0.04 wl	0.4 λ_0	60

Fig. 22 Determination of # of surfaces for Monte Carlo simulation.
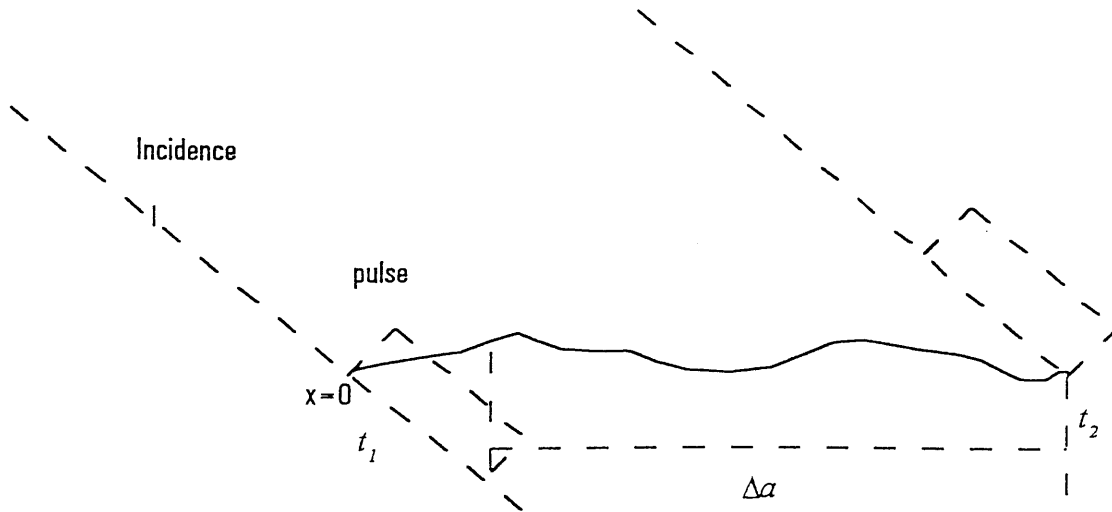
Fig. 23 Parameter calculation for the RCS parameters.

In Table 4, we compare the averaged RCS with the analytical results of the same rms height and correlation length presented in Table 3. We also plot out in Fig. 24 the comparison of the two methods. As can be seen, the results from the two methods match very well, which validates the correctness of our simulation algorithm under the small perturbation condition. In fact, in small perturbation condition, the multiple scattering between the illuminated and unilluminated regions is negligible, which is exactly the assumption we make in our simulation scheme. In Table 5, we list the RCS at incidence angles of 79, 82 and 85 degrees due to rougher surface of rms height $0.1\lambda_0$ and correlation length $0.5\lambda_0$ as compared to the SPM approximation under the same condition, there are observable big difference between the two. This, however, is not at all surprising, because at such rough surface conditions, the approximations made in the SPM analytical approximation is no longer valid.

Table 4 Comparison of the simulation result and SPM.

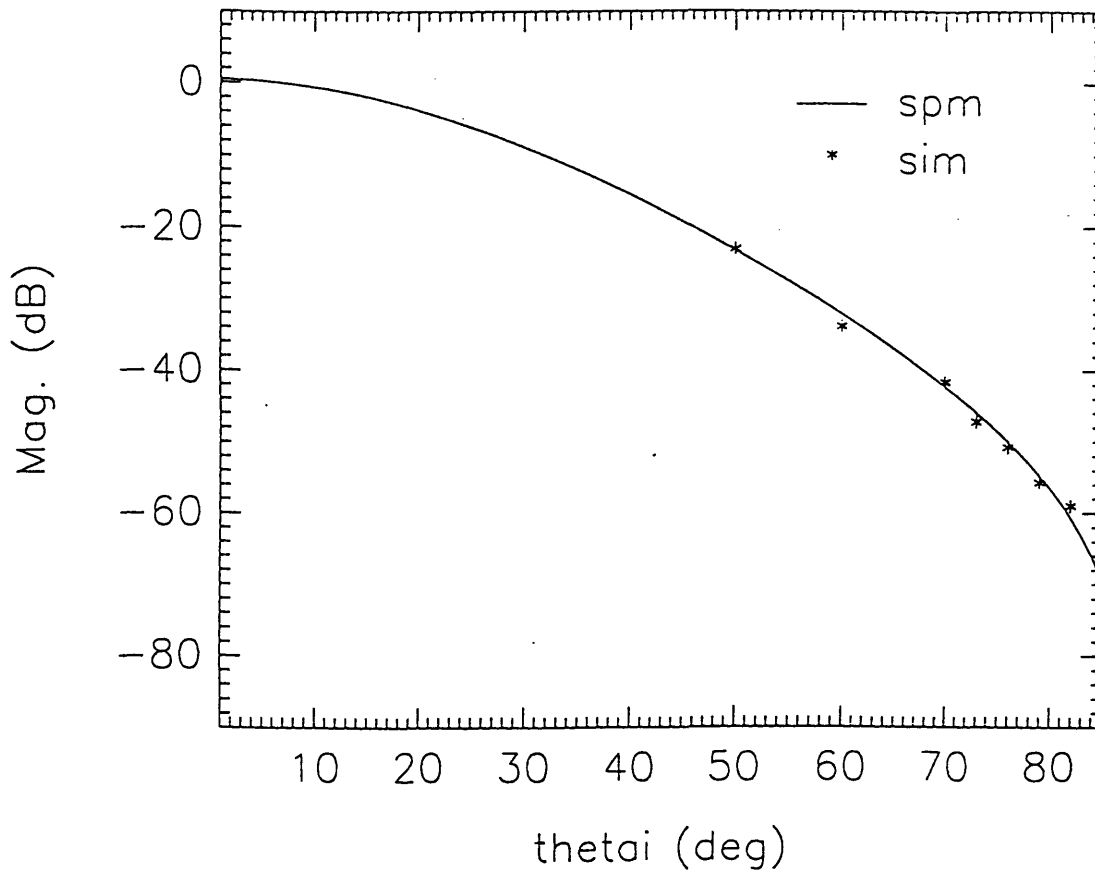| Inc. Angle (Deg)	Simulation (dB)	SPM (dB)
50	-23.04	-23.28
60	-33.86	-32.12
70	-41.65	-42.37
73	-47.22	-45.96
76	-50.72	-49.99
79	-55.67	-54.72
82	-58.96	-60.67
85	-70.32	-69.12

Fig. 24 Comparison of the simulation result and SPM.

Table 5 Simulation results for rougher surface

Inc. Angle (Deg)	Simulation (dB)	SPM (dB)
79	-46.94	-60.69
82	-52.15	-66.9
85	-62.6	-75.5

Chapter 5 Conclusion and Future Work

5.1 Conclusion

The tapering technique is used to limit illumination area in Monte Carlo simulation of rough surface scattering for near normal incidence. This technique, however, fails to work well at grazing angle illumination. In contrast, using a pulse-compression technique, we can generate plane wave pulse that illuminates only a finite segment in time.

Thus, we first decompose the time plane wave pulse into frequency components. With the consideration of the mainlobe bandwidth and the peak sidelobe value, we choose Hamming window as our plane wave pulse form. The scattering return is calculated at each frequency component using MOM. Then some basic signal processing technique is used to extract the envelop of time signal without the carrier frequency. The processed time signal is then used to obtain the RCS. The Monte Carlo methods are used next, where we apply the simulation procedure for each rough surface realization and average the results.

The verification of simulation scheme consists of three steps. We first validate the correctness of our time processing scheme by comparing the original synthesized time signal with the carrier frequency and processed signal without the carrier frequency. Then range gating idea is verified in which we compare the processed time return signal of a large plate and a small plate. The latter is just the truncated segment of the former. The results are just as what we expected theoretically. Finally, the Monte Carlo methods are used with our simulation scheme to compare against the SPM analytical results. As can be

seen in Table 4 and Fig. 24, the simulation result matches the analytical result well. This verifies the correctness of our simulation scheme.

As a suggestion for future applications, we propose a combined area limiting scheme for 2D rough surface based on the observation that the tapered illumination area only increases in the direction of incidence as the incident angle goes to grazing. Basically, we use the tapering technique normal to the incidence plane and pulse compression along the direction of incidence, i.e. transversally tapered plane wave pulse.

5.2 Future Work

The 1D scattering area limiting scheme discussed above can be extended to 2D by combining spatial taper and pulse compression techniques. In this section, we will discuss the area limiting scheme for 2D rough surface scattering.

We observed before that the tapering technique is quite useful for area limiting in rough surface scattering. For example, the formula for 2D tapering of Gaussian beam was used in [17].

$$\overline{E}_{inc}(x,y,z) = \int_{-\infty}^{\infty} dk_{x1} \int_{-\infty}^{\infty} dk_{y1} e^{ik_{x1}x + ik_{y1}y - ik_{z1}z} E(k_{x1}, k_{y1}) \, \hat{a}\,(-k_{z1}) \tag{87}$$

where $\hat{a}\,(-k_{z1})$ is the unit vector depending on the incident direction of the plane wave and the polarization. $E(k_{x1}, k_{y1})$ is the spatial spectrum which can be obtained as

$$E(k_{x1}, k_{y1}) = \frac{1}{4\pi^2} \int_{-\infty}^{\infty} dx \int_{-\infty}^{\infty} dy \, e^{-ik_{x1}x - ik_{y1}y} e^{[(ik_x x + ik_y y)(1+w)] - p^2} \tag{88}$$

with

$$w = \frac{1}{k^2} \left[\frac{1}{g^2 \cos^2 \theta_i} (2 t_x - 1) + \frac{1}{g^2} (2 t_y - 1) \right]$$

and

$$p^2 = t_x + t_y, \quad t_x = \frac{x^2}{g^2}, \quad t_y = \frac{y^2}{g^2}$$

The basic idea behind the tapering technique is to use the linear combination of plane waves incident in different directions to achieve area limiting effect so that the component fields outside the limited region cancel each other and have negligible magnitude. The tapering technique works well when the incident angle is near normal. However, the area limiting is less and less effective as the incident angle goes to grazing, which can be illustrated in Fig. 25. But it is observed that the limited area only increases in the direction of incidence, while almost remains the same in the direction normal to the incidence plane. This suggests another possible area limiting scheme when the plane wave pulse is combined, which can limit the illumination area along the direction of incidence. Noticing that the other tapering forms besides the Gaussian form are also available, we can introduce the area limiting scheme at grazing angle incidence for 2D rough surface, i.e. the plane wave pulse time compression and the Hamming space windowing is combined to achieve the area limiting effect.
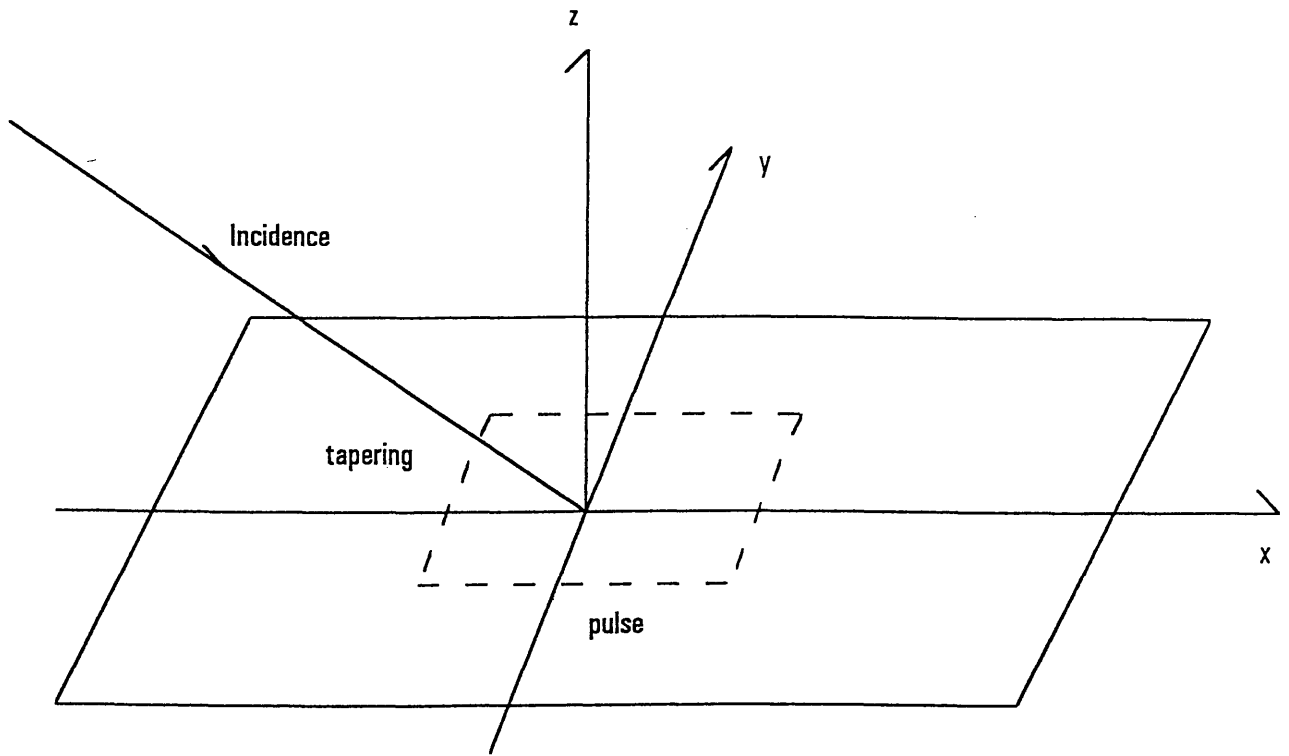
Fig. 25 Area limiting configuration for 2D rough surface.

As discussed in Chapter 3, the Hamming plane wave pulse can be expressed as

$$a_m(t) = cos\ [\omega_o(t\text{-}\hat{k}\cdot\overline{r}/c)]\ \{0.54\text{+}0.46\ cos\ [(2\pi/\tau)\ (t\text{-}\hat{k}\cdot\overline{r}/c)]\} \qquad (89)$$

$$[u(\ t\text{-}\hat{k}\cdot\overline{r}/c\text{+}\tau/2) - u(\ t\text{-}\hat{k}\cdot\overline{r}/c\text{-}\tau/2)]$$

If we add the Hamming space limiting term we can have

$$a_m(t) = cos[\omega_o(t\text{-}\hat{k}\cdot\overline{r}/c)]\ \{0.54\text{+}0.46\ cos\ [(2\pi/\tau)\ (t\text{-}\hat{k}\cdot\overline{r}/c)]\} \qquad (90)$$

$$[u(\ t\text{-}\hat{k}\cdot\overline{r}/c\text{+}\tau/2) - u(\ t\text{-}\hat{k}\cdot\overline{r}/c\text{-}\tau/2)]\ [0.54\ +0.46\ cos\ (y/a_y)][u(a\text{+}a_y)\text{-}u(a\text{-}a_y)]$$

where a_y is the tapering parameter. We can obtain the Fourier transform of (90) as

$$p_m(x, y, \omega) = e^{i k_{fx} x} H_m(\omega) s_m(y) \qquad (91)$$

where $k_{fx} = \omega/c \, \hat{k} \cdot \hat{x}$, $H_m(\omega)$ is given by (63) and $s_m(y)$ is presented as

$$s_m(y) = [0.54 + 0.46 \cos(y/a_y)] [u(y + a_y/2) - u(y - a_y/2)]$$

Now we can find the spectrum to be

$$P_m(k_{x1}, k_{y1}, \omega) = \frac{1}{4\pi^2} \int_{-\infty}^{\infty} dx \int_{-\infty}^{\infty} dy \, p_m(x, y, \omega) \, e^{-ik_{x1}x - ik_{y1}y} = H_m(\omega) \, \delta(k_{x1} - k_x) \, S_m(k_{y1}) \qquad (92)$$

where

$$S_m(k_y) = \frac{0.54}{\pi} \frac{\sin(k_y a_y/2)}{k_y} + \frac{0.23}{\pi} \frac{\sin[(k_y - 2\pi/a_y) a_y/2]}{k_y - 2\pi/a_y} + \frac{0.23}{\pi} \frac{\sin[(k_y + 2\pi/a_y) a_y/2]}{k_y + 2\pi/a_y}$$

So we use the plane waves with the identical $k_{x1} = k_x$ and different k_{y1} to achieve the 1D tapering in the y direction. The incident field in space can be written as

$$\bar{A}_{inc}(x, y, z, \omega) = p \int_{-\infty}^{\infty} dk_{x1} \int_{-\infty}^{\infty} dk_{y1} \, P_m(k_{x1}, k_{y1}, \omega) \, e^{i k_{x1} x + i k_{y1} y - i k_{z1} z} \, \hat{a}(-k_{z1}) \qquad (93)$$

$$= p \, e^{i k_x x} H_m(\omega) \int_{-\infty}^{\infty} dk_{y1} \, S_m(k_{y1}) \, e^{i k_{y1} y - i k_{z1} z} \, \hat{a}(-k_{z1})$$

where coefficient p and $\hat{a}(-k_{z1})$ are polarization dependent.

With the transversally tapered plane wave in (93) at different frequencies, we can follow the same pulse compression techniques in Chapter 3 and obtain the scattering

References

[1]   Kong, J. A., *Electromagnetic Wave Theory*. New York: Wiley, 1990.

[2]   Eftimiu, C. and Welland, G. V., "The use of Padé Approximants in rough Surface
        Scattering," *IEEE Trans. Ant. and Prop.*, vol. AP-35, no. 6, pp. 721-727, 1987.

[3]   Benali, A., Chandezon, J. and Fontaine, J., "A new theory for scattering of
        electromagnetic waves from conducting or dielectric rough surfaces," *IEEE Trans.
        Ant. and Prop.*, vol. 40, no. 2 , pp. 141-148, 1992.

[4]   Butler, C. M., Wilton, D. R. and Glisson, A. W., *Numerical Methods in
        Electromagnetics*, Lecture Notes, University of Mississippi, 1982.

[5]   Saillard, M. and Maystre, D., "Scattering from random rough surfaces: a beam
        simulation method," *J. Opt.*, vol. 19, no. 4, pp. 173-176, 1988.

[6]   Ngo, H. D. and Rino, C. L., "Application of beam simulation to scattering at low
        grazing angles 1. method and validation," *Radio Science*, vol. 29, no. 6, pp.
        1365- 1379, Nov.-Dec., 1994.

[7]   Hovanessian, S. A., *Radar System Design and Analysis*. Massachusetts: Artech
        House, 1985.

[8]   Chelton, D. B., Walsh, E. J. and Macarthur, J. L., "Pulse compression and sea
        level tracking in satellite altimetry," *J. Atmosp. and Oc. Tech.*, vol. 6, Iss. 3, pp.
        407-438, 1989.

[9]   Mittra, R. and Ramahi, O.," Absorbing Boundary Conditions for Direct Solution
        Partial Differential Equation Arising in Electromagnetic Scattering Problems,",
        *PIER 2: Finite Element and Finite Difference Methods in Electromagnetic
        Scattering*, M. A. Morgan, ed., Elsevier, New York, 1990.

[10]   Yan, J., Gordon, R. K. and Kishk, A. A., "Electromagnetic Scattering from
        Impedance Elliptic Cylinders Using Finite Difference Method (Oblique
Incidence)," *Electromagnetics,* Vol. 15, pp. 157-173, No. 2, March-April 1995.

[11]   Collins, J. D., Volakis, J. L. and Jin, J. M., "A Combined Finite Element-
        Boundary Integral Formulation for Solution of Two-Dimensional Scattering
        Problems via CGFFT," *IEEE Trans. Antennas Propagat.,* vol. 38, pp. 1852-
        1858, No. 11, Nov. 1990.

[12]   Cangellaris, A. C. and Lee, R., "Finite Element Analysis of Electromagnetic
        Scattering from Inhomogeneous Cylinders at Oblique Incidence," *IEEE Trans.
        Antennas Propagat.,* vol. 39, pp. 645-650, No. 5, May 1991.

[13]   Gordon, R. K. and Lee, J. F., "A Finite Element Method That Employs an
        Absorbing Boundary Condition for Determining the Electromagnetic Scattering by
        Inhomogeneous Cylindrical Structures That Are Illuminated by an Obliquely
        Incident Field," *IEEE Trans. Magnetics,* vol. 29, pp. 1820-25, Iss. 2, March
        1993.

[14]   Johnson, J. T., Kong, J. A. and Shin, R. T., "Polarimetric thermal emission from
        rough ocean surfaces," *J. Electromag. Waves Applic.,* vol. 5, no. 9, pp. 43-59,
        1994.

[15]   Tsang, L., Mandt, C. E. and Ding, K. H., "Monte Carlo simulations of the
        extinction rate of dense media with randomly distributed dielectric spheres based
on   solution of Maxwell's equations," Opt. Letters, vol. 17, no. 5, pp. 314-316, 1992.

[16]   Chen, M. F. and Fung, A. K., "A numerical study of the regions of validity of the
        Kirhoff and small-perturbation rough surface scattering models," *Radio Science,*
        vol. 23, no. 2, pp. 163-170, March-April 1988.

[17]   Pak, K., Tsang, L. and Hsu, C. C., "Backscattering Enhancement of Vector
        Electromagnetic Waves from Two-Dimensional Perfectly Conducting Random
        Rough Surface Based on Monte Carlo Simulations" Accepted by *J. Opt. Soc. Am.
        A.*